QATAR UNIVERSITY

COLLEGE OF ARTS AND SCIENCES

THE INFLUENCE OF SINGLE WALLED CARBON NANOTUBES ON THE THERMOELECTRIC PROPERTIES OF P-TYPE BISMUTH TELLURIDE COMPOSITE

BY

SARA MOHAMED HEGAZY

A Thesis Submitted to

the College of Arts and Sciences

in Partial Fulfillment of the Requirements for the Degree of

Masters of Science in Material Science and Technology

January 2023

COMMITTEE PAGE

The members of the Committee approve the Thesis of

Sara Hegazy defended on 09/01/2023.

Dr. Khaled Yousef
Thesis/Dissertation Supervisor

Dr. Ahmed Abdala
Committee Member

Dr. Aboubakr Abdullah
Committee Member

Dr. Ahmed Ayesh
Committee Member

Approved:

Ahmed Elzatahry, Dean, College of Arts and Sciences

ABSTRACT

Hegazy, Sara, M., Masters: January: 2023, Material Science and Technology

Title: THE INFLUENCE of SINGLE WALLED CARBON NANOTUBES on THE THERMOELECTRIC PROPERTIES of P-TYPE BISMUTH TELLURIDE COMPOSITES

Supervisor of Thesis: Dr. Khaled,M.,Youssef.

The most important thermoelectric materials for applications close to room temperature are made of bismuth telluride. The number of applications for these materials, however, is constrained by their extremely low heat conversion efficiencies. Single Walled Carbon Nanotubes (SWCNTs) are employed as a nanofiller in this work to create a p-type bismuth telluride nanocomposite with the composition $Bi_{0.4}Sb_{1.6}Te_3$. Ball milling was used to prepare the samples with various SWCNTs concentrations for a total milling time of 16 hours. According to the findings, the addition of SWCNTs enhanced the thermoelectric characteristics of p-type bismuth telluride. The addition of SWCNTs raised ZT at room temperature by 5% (from 0.86 to 0.90) for the optimal sample (0.05 wt.% SWCNTs),. At 150 °C, ZT improved by 4 %, achieving a value of 1.26 for the same sample (0.05 wt.% SWCNTs). Consequently, demonstrating that SWCNTs may improve the thermoelectric characteristics of the p-type bismuth telluride samples.

DEDICATION

This work I dedicate entirely to my respected parents and my dear sister since it would not have been possible without their ongoing support. They continually inspire me. Along with that, I want to thank my thesis advisors and mentors, under whose steady supervision I accomplished my thesis.

ACKNOWLEDGMENTS

I'd like to sincerely Thank Dr. Khaled Youssef, my thesis supervisor, for allowing me to complete my thesis under his supervision and for his ongoing academic guidance and support.

Special appreciation to Eng. Farah El-Makaty for her sincere guidance and assistance with the thesis experimental work.

In addition, I'd like to thank the members of my thesis committee, Dr. Ahmed Abdala, Dr. Aboubakr Abdullah, and Dr. Ahmad Ayesh, for their insightful remarks and suggestions.

This work has been made possible thanks to grants no. NPRP10 0206 170366 from the Qatar National Research Fund and the Qatar Foundation, respectively. Special appreciation is extended to the University of Qatar's Centre of Advanced Materials and Central Laboratory Unit for their cooperation with the experimental work. Specifically, Dr. Peter Kasak, Mr. Abdulla Al Ashraf, Mr. Abdul Jaleel Naushad, Dr. Mohamed Ahmed, Mr. Essam Attia, Dr. Nandagopal Pothuvattil, Ms. Muneera Al-Qahtani, Eng. Sherin Mohamed and Mr. Tageldin Reda.

Thank you to the external examiner, for his insightful and welcomed remarks on the thesis. Lastly, I wish to convey my heartfelt gratitude to the teaching members of the Materials Science and Technology Master Program who provided me with a multitude of beneficial courses during my Master of Science studies.

LIST OF TABLES:

LIST OF FIGURES

CHAPTER 1: INTRODUCTION

Global warming is being growing dramatically in the last 10 years and this is noticeable on the climate change. There are many reasons beside the major effects of greenhouse gases to contribute in increasing climate's temperature. Waste heat energy which is lost in the air by fossil fuels combustions where stated that it is the dominating reason for global warming. (Bian, 2020)Figure 1 is showing the linear relationship between the waste heats entered environment versus the carbon dioxide according to the regression coefficient which equals to 0.98. This means that when waste heat increases, CO_2 increases and global warming increases(Bian, 2020).

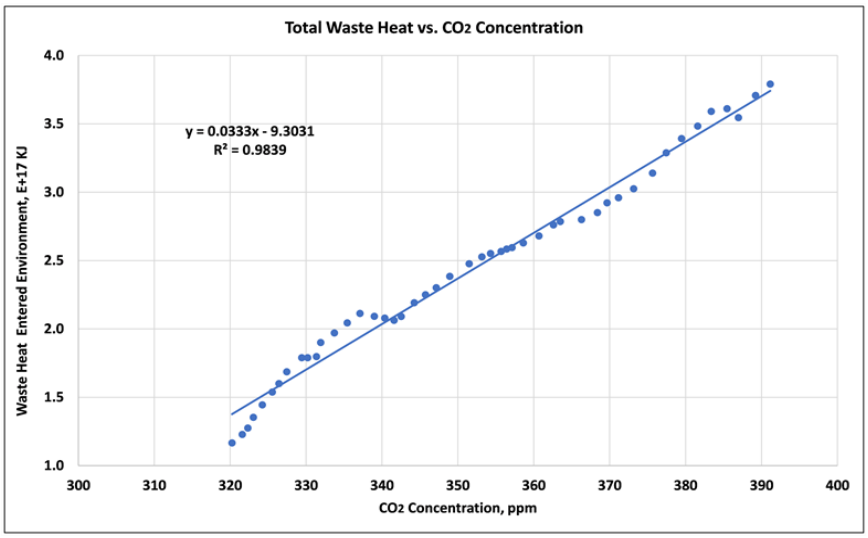

Figure 1:The relationship between Waste Heat versus CO2 concentration(Bian, 2020)

Besides global warming effect, there are a huge demand on the electrical energy in the world's continents according to the population growth(Dimitriev & Lashkaryov, 2013). It has been mentioned that the energy consumption is growing larger than the population growth by an annual increase of 1.9% which means people are demanding and consuming energy more than past decades as shown in Figure 2(Dimitriev & Lashkaryov, 2013).

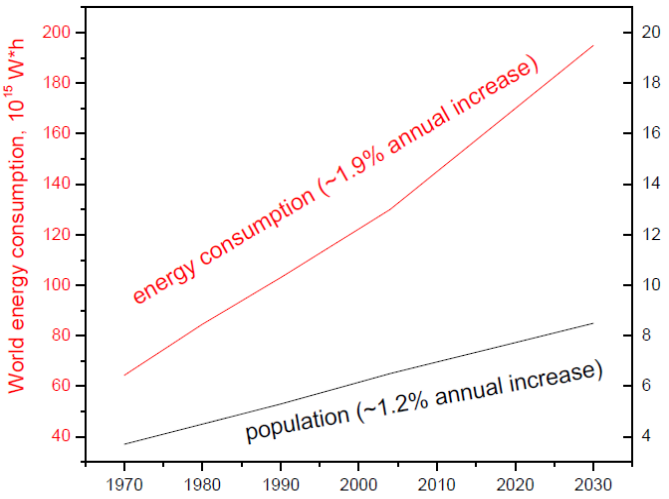

Figure 2:The annual increase for World energy consumption versus populationor World energy consumption versus population(Dimitriev & Lashkaryov, 2013)

Utilizing the thermoelectric materials (TE) as a possible approach to transform waste heat into electrical energy it will reduce the consumption of energy. There are many advantages for using TE materials since they are having no moving parts, no pollutants and no noise. The performance and efficiency of TE materials is being enhanced and improved by using ZT or the figure-of-merit. There are many diverse materials to be used in applications near room temperature and one of them is the bismuth telluride Bi_2Te_3 (Kanatzidis, 2009a; Nozariasbmarz et al., 2020a; Tan et al., 2019b). Bi_2Te_3 alloys are utilized in the medical applications, transportation, power generation and aerospace (Figure 3)[4]–[7].

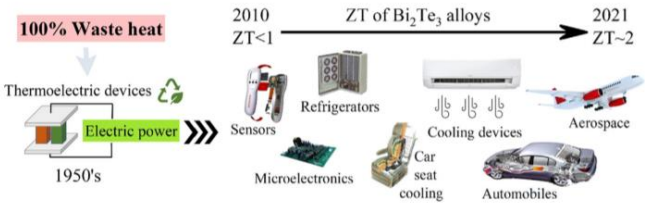

Figure 3:Thermoelectric applications of bismuth telluride alloys(El-Makaty et al., 2021)

The dependency of how efficient the heat energy is converted to electrical energy by the use of (TE) materials is dependent on ZT which is known as $\alpha^2\sigma\kappa^{-1}$T, in which α is for Seebeck coefficient, σ is for electrical conductivity, κ is for thermal conductivity and T is for absolute temperature. The Seebeck coefficient might be altered to produce a different ZT value by increasing the material's electrical conductivity while simultaneously decreasing its thermal conductivity. There are two ways to get to this point: one is an intrinsic approach called nanostructuring, and the other is an extrinsic one called compositing. Both of these techniques are intended to improve the thermoelectric property. Nanostructuring lowers heat conductivity by increasing the phonon scattering in the nano-grain boundaries. These nano-grain boundaries may be changed using powdering metallurgical techniques like as hot pressing and chemical synthesis, both of which produce nanotubes and nanoparticles (B et al., 2008; Dresselhaus et al., 2007; Scheele et al., 2009; Takashiri et al., 2007; Tang et al., 2007; Xie et al., 2009a; Zhao et al., 2005a).

Most of the time, the TE device is made-up of p-type and n-type materials, which is sandwiched between two insulator plates and connected electrically in series (or partially parallel) and thermally in parallel (usually polymers or ceramics). Figure 4a, b, c shows the thermoelectric device types. Figure 4a. represents the π -shaped configuration of TE module. The two most popular shapes are Y-shaped and tube-shaped modules. Weinberg demonstrated a tube-shaped TE module in 2002 that has a ring-shaped heat source surrounded by alternate n-type and p-type TE elements (Figure 4b) (*Thermoelectric Materials and Devices - Lidong Chen, Ruiheng Liu, Xui Shi -*

Google Books, n.d.). Figure 4c illustrates the Y-shaped configuration that Bell adopted in 2006 [3].

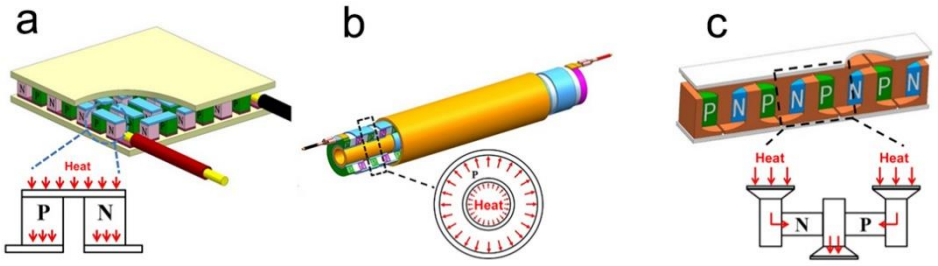

Figure 4:a) Structural diagram of the π-shaped TE module, b) the tube-shaped TE module, c) Y-shaped TE module(Chen et al., 2021)(*Thermoelectric Materials and Devices - 1st Edition*, n.d.)

Different cross-sectional areas and thicknesses of TE elements can fit in this Y-shaped arrangement more easily. The p-type and n-type thermoelectric elements are placed next to each other, with an electrode in between each pair. In a cornering transfer path, the electrodes also make it easier for heat to move from the source of heat to the side TE elements. This Y-shaped structure makes it possible to combine TE elements with free-form geometries. This means that different sizes and forms can be created for p-type and n-type elements.

The figure of merit value is utilized to describe how well a thermoelectric device works. It is defined as:

$$ZT = \frac{S^2 \sigma T}{\kappa} \quad (1)$$

As shown in equation 1 the abbreviated terminology to define ZT is that Seebeck coefficient to define the letter S and the electrical conductivity,the absolute temperature and the thermal conductivity are to define respectively the letters $\sigma, Tand\ \kappa$. Thermal conductivity consist of two parameters the electronic thermal conductivity and the

lattice thermal conductivity which are (κ_E) and (κ_L) respectively and the $S^2\sigma$ is to define the thermoelectric power factor (PF)(Pezzoli et al., 2011).

When there is a potential difference ΔV occur is built up across a semiconductor according to the carrier diffusion and the temperature gradient by $T=T_{(hot)}-T_{(cold)}$ as one material is heated or cooled, all these phenomena is refered to "Seebeck effect". There is a gradient in the number of charge carriers as a result of the passage of charges from the hot side to the cold side. This gradient is balanced out when the system is in equilibrium by the internal electrical field that is produced so as a result, in equation 2, the Seebeck coefficient is provided.

$$\alpha = -\frac{\Delta V}{\Delta T} \quad (2)$$

The majority carriers which could be electrons or holes are the determining factor for the positivity or negativity of seebeck coofecient ant the voltage difference. This means that the potential difference (and, consequently, the Seebeck coefficient) can be written as α_p is larger than zero for p-type semiconductors and α_n is lesser than zero for n-type semiconductors (Chang, R. P., & Rhee, 1990; Lenz et al., 2011; Zuo et al., 2016).

The thermoelectric material must be connected to a load in order to transform the Seebeck voltage into an electrical current (or series of materials). to increase the potential production of energy. It is necessary to minimise both the thermal losses from heat transfer in between hot and cold reservoirs and the electrical losses from Joule heating. The thermoelectric material must thus be both extremely thermally inefficient and highly electrically conductive. Comparing the thermoelectric efficiency of various materials is made possible by the so-called thermoelectric figure of merit ZT, which takes into consideration the need for a high Seebeck coefficient, high electrical conductivity, and low thermal conductivity.

The thermal conductivity of a material is further divided into two components by the equation: κ =κE + κL, where κE and κL stand for, respectively, the electronic thermal conductivity and lattice thermal conductivity (equations 4,5)(FJ, 1999). The electrical conductivity (σ) and electronic thermal conductivity (κe) often increase as carrier concentration rises, whereas the Seebeck coefficient (S) generally decreases (Snyder & Toberer, 2008). In thermoelectric, thermal conductivity is created by both heat-carrying electrons and holes (κE) and phonons moving across the lattice (κL). The bulk of the electronic term (E) is connected to electrical conductivity by the Wiedemann-Franz law:

$$\kappa = \kappa_e + \kappa_L \quad and \quad \kappa_e = L\sigma T = ne\mu LT \tag{3,4}$$

where L is the Lorenz factor, 2.4×10^{-8} J ^{2} K^{-2} C^{-2} for free electrons (*Applications of Thermoelectricity / H.J. Goldsmid. - University of Queensland*, n.d.).According to equation 5, the electrical conductivity is directly related to the charge carrier mobility (μ), charge carrier concentration (n), and charge of the carrier (e), all of which are affecting the material's electrical band structure.

$$\sigma = ne\mu \tag{5}$$

Additionally, as indicated in equation (6), the mobility of charge carriers is made up of the mobility of the carriers in the matrix ($\mu matrix$) and the mobility of the carriers at the interface ($\mu_{\text{interface}}$):

$$\frac{1}{\mu_{\text{Total}}} = \frac{1}{\mu_{\text{matrix}}} + \frac{1}{\mu_{\text{interface}}} \tag{6}$$

And the definition of the mobility at the interface is:

$$\mu_{\text{interface}} = \text{Le}\left(\frac{1}{2\pi m^* k_B T}\right)^{\frac{1}{2}} exp\left(-\frac{E_B}{k_B T}\right) \tag{7}$$

where L is for the distance between two adjacent interfaces, m* is the effective mass of the carrier, kB is the Boltzmann Constant, T is the absolute temperature and E_B is the potential barrier height(Kumar et al., 2018). Equation (7) makes it clear that high temperatures will decrease interface mobility, hence reducing overall mobility. The figure of merit progressively risen in the second part of the twentieth century. This was the outcome of the usage of semiconducting materials with improved electrical properties and reduced lattice thermal conductivity. By enhancing phonon scattering (through lowering the lattice thermal conductivity) (Goldsmid, 2021).Solid solution formation is one of the most effective methods for decreasing lattice thermal conductivity (*Scholar (29)*, n.d.).By decreasing the size of the crystal, it is also possible to reduce the lattice's thermal conductivity. In the majority of materials, phonons are primarily scattered by other phonons (Azhar, 2007).Due to a scattering mechanism at the grain boundary, it has been discovered that increasing the number of grain boundaries decreases thermal conductivity(Li et al., 2017). Although several thermoelectric materials have been explored, their ZT values are quite low, making bismuth-telluride-based alloys essential for applications that need operation at or close to room temperature (Kanatzidis, 2010). Recent nano-based procedures for preparing bismuth telluride materials have opened up new possibilities for improving its thermoelectric characteristics. There is a substantial difference between the commercial applications of antimony doped bismuth telluride and its n-type counterpart, selenium doped bismuth telluride, whose ZT at room temperature is significantly lower than 1. However, its p-type antimony doped bismuth telluride exhibits high ZT values of nearly 1.5 (Fan et al., 2010; Xie et al., 2009c),(*Improvement in Thermoelectric Properties of N-Type Bismuth Telluride Nanopowders by Hydrogen Reduction Treatment*, n.d.).

According to a number of research, nanocompositing and nanostructuring may be used to increase the ZT of thermoelectric materials.

Ball milling has been shown to boost the figure-of-merit value and is a relatively affordable and practical nanostructuring technology (Mamur et al., 2018). However, to get better materials, it is essential to optimize the milling time. When components or materials other than bismuth telluride are added to bismuth telluride, either an alloy or a composite is produced. It is generally known that this is an effective method for increasing the thermoelectric characteristics of the material. The impact of each category, however, might be somewhat different depending on the particular microstructure that is created. The production of materials with better qualities that cannot be produced with individual components is made possible via the use of an innovative method known as nano compositing. Nanocomposites are made up of a matrix (such as an alloy of bismuth telluride, for example) and a nanofiller. The induced selective scattering at the new interfacial regions generated between the matrix and the nanofiller is the essential concept that supports the process of nano compositing. Due to the presence of this property, it is feasible to significantly decrease the thermal conductivity of the material without substantially reducing the electrical properties (El-Makaty et al., 2021).

SWCNTs (Figure 5) are classified as 1D materials due to their tiny diameter. They are called that because their structure is hollow and they have many walls. They are used in many ways right now, like as supports for catalysts, materials for thermal interfaces, solar, biomedical, and wearable electronics (Nanot et al., 2013). CNTs are thought to be almost one-dimensional structures. SWCNTs and MWCNTs are the two most common types of carbon nanotubes. One graphene sheet is wrapped around a single cylinder in a SWCNTs. MWCNTs are just SWCNTs arranged in a ring. There is

a wide range in the length, diameter, and other properties of these structures(Rakhi, 2019). It looks like a hexagonally arranged tubular graphene shell consisting of carbon atoms. Figure 6 shows how pure SWCNT looks. SWCNTs are usually made up of just 10 atoms around the outside and one atom in the middle. Carbon nanotubes can be divided into three types, in addition to the two main types. Carbon nanotubes (CNTs) are composed of armchair, zigzag, and chiral CNTs. These three CNT varieties exist. How the graphite is "rolled up" during the manufacturing process determines how these two forms of carbon nanotubes differ from one another. There are different types of SWCNTs that can be made because of the radius and direction of the rolling axis. Carbon nanotubes are very strong because of the strength of the Sp2 carbon-carbon bonds. No other material has shown that it has better mechanical, thermal, and electrical qualities than they do. In terms of weight, their density could be anywhere from 1.3 kg/cm3 to 1.3 kg/cm3 (one-sixth of that of stainless steel)(Saifuddin et al., 2013). Compared to steel, the Young's moduli of CNTs are five times bigger, making them stiffer than all carbon fibers. This makes them better than all other carbon fibers (Yu et al., 2000). Because of this, though, they are truly unique among their peers. Too far, no other substance has been as effective as carbon nanotubes. As of now, the carbon nanotube has the greatest recorded tensile strength or breaking strain, which is about 50 times stronger than steel(Yu et al., 2000). In addition, CNTs have excellent chemical and environmental stability, as well as strong thermal conductivity (about 3000 W/m/K)(Saifuddin et al., 2013). The addition of CNTs to the Bi2Te3 matrix results in wide and distinctive interfaces, which acts as a thermal barrier, resulting in high ZT values. These findings show that incorporating CNTs into thermoelectric materials holds great promise for achieving a high merit score (ZT). In the temperature range of 298–498 K, the composite's dimensionless figure of merit (ZT) exhibits much higher

values than those of pure binary Bi2Te3, and at 473 K, a ZT of 0.85 was the highest possible. The lower heat conductivity at the CNT/Bi2Te3 interface, as a result of active phonon-scattering, is thought to be the primary cause of the composite's enhanced thermoelectric performance (K. T. Kim et al., 2013b).

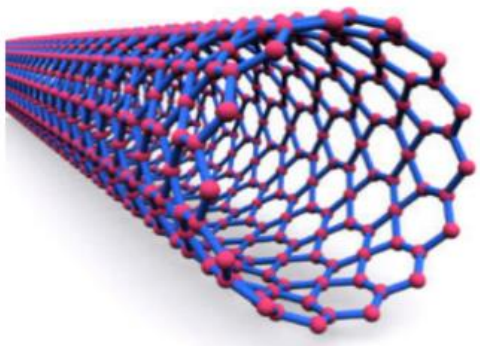

Figure 5: Single walled carbon nanotubes[40]

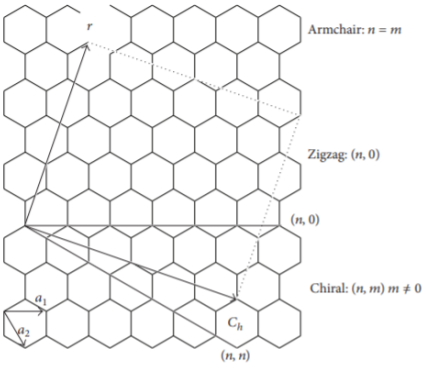

Figure 6:Representation of SWCNT [37]

$Bi_{0.4}Sb_{1.6}Te_3$ and a thermoelectric ZT value above 1 is the main purpose of this study, which aims to create a very efficient-type bismuth telluride with single-walled carbon nanotubes. Two methods are mentioned as being used to achieve this goal, the first of which is to improve the thermoelectric properties of the nanostructured p-type bismuth telluride alloy by ball milling in order to reach the desired ZT ratio. By decreasing the grain size through nanostructuring and adding a nanofiller (SWCNTs) via nanocompositing, it is believed that the thermoelectric properties of the p-type $Bi_{0.4}Sb_{1.6}Te_3$ can be improved.

Research Questions

During this research, the following questions were examined:

1. What is the effect of nanostructuring on the thermoelectric characteristics of p-type bismuth telluride?

2. What is the influence of SWCNT on the thermoelectric properties and the ZT value of p-type bismuth telluride nanocomposite?

CHAPTER 2: LITERATURE REVIEW

THERMOELECTRIC BISMUTH TELLURIDE:

Bismuth Telluride (Bi_2Te_3) is regarded as one of the most important materials in thermoelectric materials since it has the ability to convert the waste thermal energy to electrical form of energy (Culebras et al., 2015). Bismuth telluride has a high mean atomic weight, a low melting temperature of 585°C, and a low lattice conductivity, in addition to its chemical characteristics (Ioffe & Ioffe, 1954; Keyes, 1959). Many efforts have been conducted in recent years to create high efficiency thermoelectric materials using the Bi_2Te_3 nanostructure (Antonenko et al., 2017; Culebras et al., 2017; Gaul et al., 2017; Lee et al., 2017; Luo et al., 2016; Mahmud et al., 2017; Wu et al., 2017; C. Zhang et al., 2017).

A number of applications can be used with Bi_2Te_3, including thermoelectric refrigeration, thermoelectric generators, thermoelectric converters, and thermal sensors, among others(Akshay et al., 2017; Erickson et al., 2017; Fang et al., 2015; Gaikwad et al., 2016; Jian et al., 2017; Loa et al., 2016; Sharma et al., 2016; Talebi et al., 2017). The Figure of Merit, also referred to as ZT, is 0.84 for n-types and 1.08 for p-types(*A. F. Ioffe Semiconductor Thermoelements And Thermoelectric Cooling Infosearch (1957) : Free Download, Borrow, and Streaming : Internet Archive*, n.d.; Nozariasbmarz et al., 2020b),(Brostow et al., 2012). In order to increase the thermoelectric properties of Bi_2Te_3, many studies on their applications have lately been undertaken. When materials are produced into nanostructure dimensions, their figure of merit is significantly increased (Goldsmid, 2014; Hines et al., 2012; Khodiri et al., n.d.; Orr et al., 2016; Rodríguez-Fernández et al., 2016; Saleemi et al., 2011; Technology, n.d.).Nanostructures having one or more reduced dimensions, such as nanowire, nanoplates, nanotubes, nanorods, nanosheets, and nanoflowers, have recently

been used to improve the performance of Bi_2Te_3 materials(Deng et al., 2002). Bismuth telluride is a semiconductor that has an extremely tiny gap[47]. Since Bi_2Te_3 has Van der Waals links between neighbouring tellurium atoms, it is easy to break apart in this direction. A bismuth, antimony, tellurium, and selenium alloy must be used in power-generation devices to rectify the Seebeck coefficient of bulk Bi_2Te_3 (Satterthwaite & R. W. Ure, 1957). Due to Van der Waals links between neighboring tellurium atoms, Bi_2Te_3 is easily crumbled in this direction. For power-generation devices, bismuth, antimony, tellurium, and selenium alloys must be used to rectify the Seebeck coefficient of bulk Bi_2Te_3. As seen in Figure 7, Bi2Te3 crystallizes as a rhombohedral crystal with five atoms in each unit cell. Due to their respective atomic weights of seven and four times that of silicon, bismuth and tellurium can be used as thermoelectric substances. It consists of five layers that repeat along the z-axis (Te'-Bi-Te'-Bi-Te')(Satterthwaite & R. W. Ure, 1957),(Kokalj, 1999),(Tanaka et al., 2009). As with regular glass, bismuth telluride has a very low lattice thermal conductivity of 1.20 W/(m•K) and a high electrical conductivity of 1.1105 S•m/m^2(Tanaka et al., 2009).

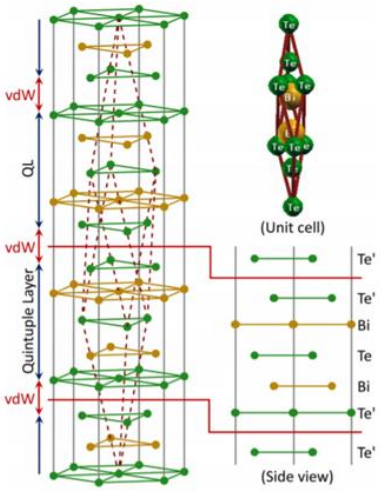

Figure 7:Crystal structure of bismuth telluride [72].

NANOSTRUCTURING

Nanostructures are defined as materials that have at least one dimension between 1 and 100 nm. Materials are given unique and specialised qualities by nanostructures while maintaining their bulk properties. Nanomaterials offer high-performance applications because of the large surface area of these structures, and they are essential to the development of new technologies. As a result, nanostructures have gained more attention in recent years in domains based on electrical, biological, chemical, physical, and optoelectrical principles. The confinement of electrons in space results in special properties that are only present at the nanoscale, and they are strongly influenced by the material's size. Recent research has been able to dramatically improve the figure of merit using nanostructuring and enhance the thermoelectric characteristics of bismuth telluride alloys [10]. The higher density of grain boundaries and interfaces is what causes ZT values in bulk nanostructured thermoelectric materials to increase. In addition to facilitating phonon scattering, they also raise the figure of merit value of the lattice by reducing the thermal conductivity. Usually, nanostructuring is performed in two ways: from the top down and from the bottom up. By linking atoms or molecules, the second process builds up a material, whereas the other divides it into nanoscale particles. Numerous studies have already examined the characteristics of Bi2Te3 thermoelectric materials produced using such methods. For instance, Takiishi et al. [19] used flash evaporation as a bottom-up approach to create nanocrystalline thin films of n-type bismuth telluride. Compared to the bulk material, the produced films' thermal conductivity was 50% lower. Additionally, Fan et al. [20] investigated the impact of nano inclusions on the ZT value of top-down melt-spun bismuth telluride nanocomposites. Researchers established that adding more weight to the thermoelectric

material's nanoinclusions decreases thermal conductivity while maintaining a higher figure-of-merit value. The use of nanostructuring is the reducing of materials that composed of nanometer size grains to solve the thermal conductivity issue while maintain the electrical conductivity(Hsu, 2004; D. J. Singh & Terasaki, 2008). Studies showed that when BiSbTe was nanostructured, the ZT value increased by nearly 50% (Bentien et al., 2007; D. J. Singh & Terasaki, 2008). The nanostructuring of thermoelectric materials and the production of nanocomposites are two methods for lowering thermal conductivity (Biswas et al., 2012; Cao et al., 2008; S. Il Kim et al., 2015; Park & Lee, 2016; Poudel et al., 2008; Sootsman et al., 2009; Venkatasubramanian et al., 2001; Xie et al., 2009b; Zhao et al., 2005b).

BALL MILLING

By using mechanical energy, ball milling reduces the material into tiny particles by using top-down nanostructuring. This method generates nano-sized alloys and solid solutions from dry powders. Nonetheless, grain refinement or phase change is the primary goal of the mechanical milling (MM) process. Grain refining occurs as a result of repetitive mechanical hits that cause severe plastic deformation, as shown in Figure 8. Milling should be done for as long as the starting material takes to attain a steady condition. The resulting power is then compacted into bulk materials using thermal treatments to analyze the microstructure and characteristics. Choosing raw materials, selecting a mechanical mill, and setting parameters for the process are the three basic components of an MM process. Metals, alloys, and refractory compounds can all be found in the first raw powders. Their size can range from 1 to 200 m, it is however recommended that raw powders be the same size as the grinding media (e.g., grinding balls).It's critical to use high purity powders because they determine the final composition, phase, and kinetics. Furthermore, there are various different types of high-

energy mills, which differ primarily in capacity, design, and efficiency. The most common shaker mill in laboratories is the SPEX mill, which moves back and forth with lateral motions up to a thousand times a minute (Suryanarayana, 2004).

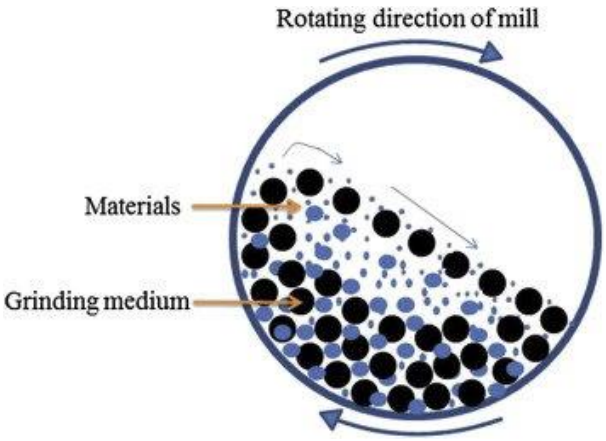

Figure 8:Dynamics of Ball Milling [87]

COMPOSITING

Compositing (Figure 9)is the process of homogeneously combining various resources to create a single material without actually blending them. The new substance contains a variety of special qualities that weren't present in any of the original materials. Typically, a matrix and a filler make up composite materials. It has been demonstrated that composing improves a material's thermoelectric characteristics. Furthermore, it has been found that utilizing various fillers with bismuth telluride as a matrix decreases the whole lattice's thermal conductivity [23]. Filler and matrix interfaces form new interfaces, causing this reduction. Also, carrier filtering and quantum confinement methods have been observed to increase the Seebeck coefficient value in these interfacial regions [24]. When different components are homogeneously blended together to make a single material without physical blending, this is referred to as composing. There is a combination of properties that are unique to the newly created substance, which have never been demonstrated by any of the previous materials.

Fillers and matrices are usually combined to form composite materials. It has been proven that combining materials improves their thermoelectric properties. Furthermore, it has been found that utilizing various fillers with bismuth telluride as a matrix reduces the overall lattice thermal conductivity (Lognoné & Gascoin, 2015). The additional contacts generated between the filler and the matrix are the cause of this reduction. Furthermore, carrier filtering or quantum confinement processes have been observed to increase the Seebeck coefficient value in these interfacial regions (K. T. Kim et al., 2013b).

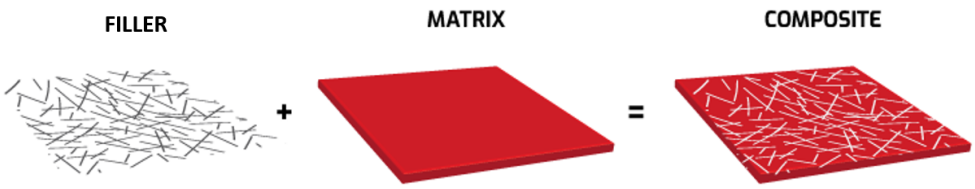

Figure 9:. How composite is made-up (*What Are Composites? - Romeo RIM*, n.d.)

SINGLE WALLED CARBON NANOTUBES:

SWCNTs (Figure 10) are defined as 1D material because of their small diameter. They are named so because they are composed of hollow structure and number of walls. They are currently used in many applications such as catalyst supports, thermal interface materials, solar, biomedical and wearable electronics (Nanot et al., 2013). SWCNTs and MWCNTs are the two primary categories of carbon nanotubes (CNTs). SWCNT is shaped like a cylinder with a single graphene sheet wrapped around it. It is simply a collection of concentric SWCNTs that make up a MWCNT (multi walls carbon

nanotubes) (Rakhi, 2019). As seen in Figure 11, the graphene sheet in pure Carbon atoms are arranged hexagonally on the surface of SWCNT to make the tubular shell. SWCNTs typically have just 10 atoms around the perimeter and a tube thickness of one atom. Carbon nanotubes can be classified into three varieties, in addition to the two basic forms. Carbon nanotubes come in three different shapes: armchair, zigzag, and chiral. As a result of the Sp2 carbon-carbon bonds, carbon nanotubes are extremely strong mechanically. As far as we know, no other material can match CNTS's combination of exceptional mechanical, thermal, and electrical properties. A density of 1.3 grams/cm^3 to 1.3 grams/cm^3 is possible (a sixth of stainless steel) (Saifuddin et al., 2013). Compared to other carbon fibers, CNTs have a greater Young's modulus than steel, an indicator of stiffness (Yu et al., 2000). Because of this, though, they are truly unique among their peers. Carbon nanotubes are the toughest substances ever discovered by humanity. The maximum tensile strength or breaking strain measured for a carbon nanotube was 63 GPa, which is approximately 50 times stronger than steel (Yu et al., 2000). Additionally, carbon nanotubes exhibit exceptional chemical and environmental stability, as well as a high thermal conductivity (about 3000 W/m/K) (Saifuddin et al., 2013). The addition of CNTs to the Bi_2Te_3 matrix results in wide and distinctive interfaces, which acts as a thermal barrier, resulting in high ZT values. These findings show that incorporating CNTs into thermoelectric materials holds great promise for achieving a high merit score (ZT). In the temperature range of 298–498 K, the composite's dimensionless figure of merit (ZT) exhibits much higher values than those of pure binary Bi_2Te_3, and at 473 K, a maximum ZT of 0.85 was attained. The lower heat conductivity at the CNT/Bi_2Te_3 interface due to active phonon scattering, is thought to be the primary cause of the composite's enhanced thermoelectric performance (K. T. Kim et al., 2013b).

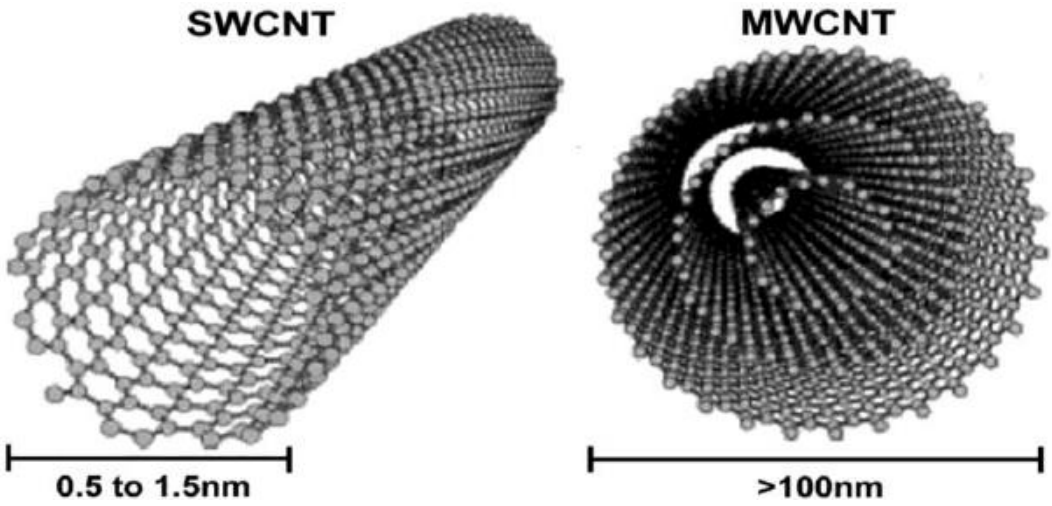

Figure 10:Single walled carbon nanotubes and Multiwalled carbon nanotubes [89]

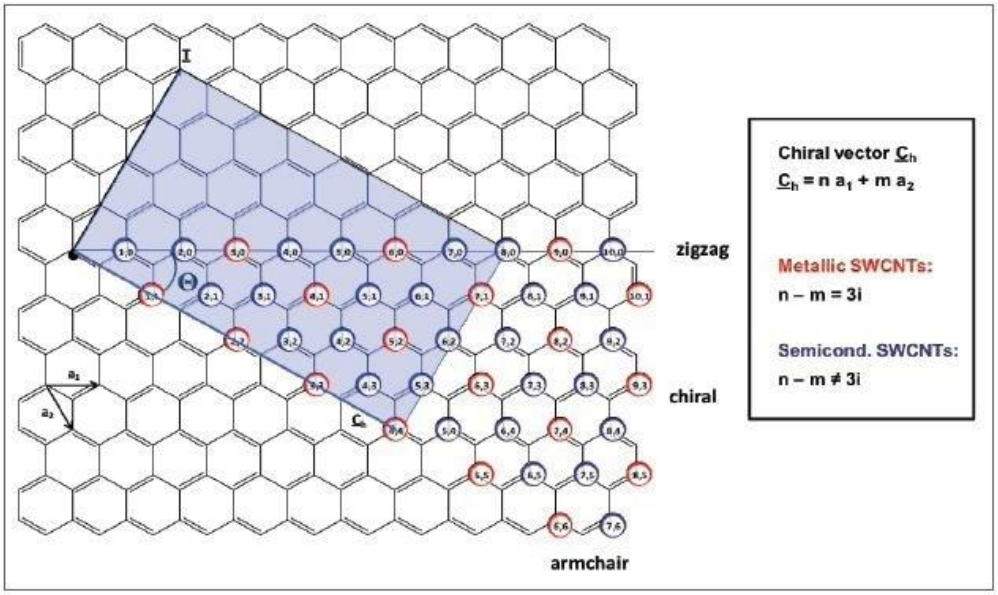

Figure 11:Representation of SWCNT [90].

CHAPTER 3: MATERIALS & METHODS

Elemental powders of bismuth (99.99%, ALDRICH), tellurium (99.997%, ALDRICH), and antimony (99.999%, Alfa Aesar) were used to produce p-type bismuth telluride alloy. In the argon atmosphere of glove box (O_2 <0.5 ppm) (LAB star, M3RAUN), the powders were weighted according to the formula $Bi_{0.4}Sb_{1.6}Te_3$ and loaded into a stainless steel vial. SPEX milling equipment (Sample Prep, 8000M, LEESON) was then used to mill the powders for 16 hours to be in the Nano scale size (Figure 12).

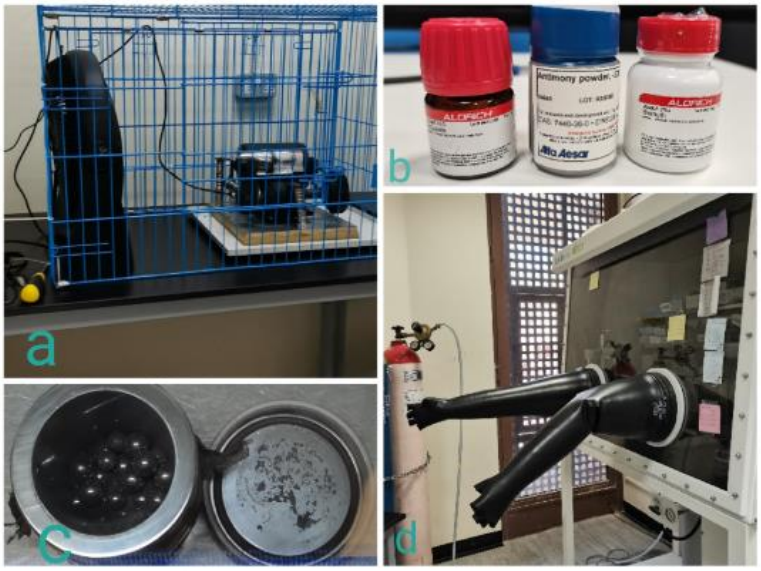

Figure 12:a) Ball milling device, b) chemicals used, c) ball milling (LEESON) vial with stainless steel balls, d) Glove box machine (M3RAUN)

The sample procedure was used to mill four different SWCNT/ $Bi_{0.4}Sb_{1.6}Te_3$ composites with different weighted percentages of SWCNT as shown in Table 1.

Table 1: Weights used to mill the SWCNTs/ $Bi_{0.4}Sb_{1.6}Te_3$ composite samples.

Elements	**0 SWCNTs (g)**	**0.025 SWCNTs (g)**	**0.05 SWCNTs (g)**	**0.1 SWCNTs (g)**
$Bi_{0.4}$	0.8850	0.8848	0.8845	0.8841
$Sb_{1.6}$	2.0625	2.0619	2.0614	2.0604
Te_3	4.0526	4.0516	4.0506	4.0485
SWCNTs	0.0000	0.0018	0.0035	0.0070
Total	7.0000	7.0000	7.0000	7.0000

The milled powders were compacted using hot press setup (Compac) shown in Figure 13 under argon atmosphere. At a pressure of 80 MPa, a temperature of 300 °C, and a holding time of five minutes, the material was compacted.

Figure 13: Hot press setup,(COMPAC)

CHARACTERIZATION:

X-ray diffraction (XRD)

X-ray diffraction is a technique for studying the structure of crystalline materials. It can provide information on crystallinity, phases, structure, and crystal defects of a material. The XRD device in Figure 14 consists of three basic parts: the X-ray source, the detector, and the sample stage. Diffraction occurs when a beam of X-rays emerges from the source and strikes the sample at an angle of 2thetas. A crystal transmits X-rays at different angles due to the distance between the atomic planes, which determines the angles of diffraction. A constructive impact occurs when the impact planes are in phase, their energy is combined, resulting in the appearance of black spots on the detection plate. Because of the rotational movement of the sample, circular patterns are formed. The radii of these patterns are utilized to compute the distance between plates inside the crystal structure. It is therefore possible to record the intensity of X-ray photons as they are reflected at various angles and turn them into a diffractogram. The conditions followed in XRD instrument were: temperature was 25℃, the voltage used was 45 KV, the current was 40 mA and the anode material was copper. All peaks are sharp which indicate there are good crystallinity of our samples(*IJMS, International Journal of Mechanics Structural, Mechanics Journals, Journals Publishers, Computer Science Journals in India, Indian Journals Subscription Agency, Indian Books Distributor*, n.d.).

Figure 14: X-ray diffraction instrument (PANalytical Empyrean) at CAM, Qatar University.

A crystal's unit cell size can be determined by calculating the distance between neighboring layers based on the result data. As a result of Braggs Law, the wavelength of an X-ray beam (L) is related to its diameter (d) by equation 8, which provides the following equations:

$$n\lambda = 2d_{hkl}\sin(\theta) \quad (8)$$

n represents the order of diffraction, λ represents the wavelength of the incident beam in nm, d_{hkl} represents the lattice spacing in nm, and θ represents the angle of the diffraction in degrees. Braggs law origin is shown schematically in Figure 15, and diffraction occurs only when an angle fulfills Braggs law.

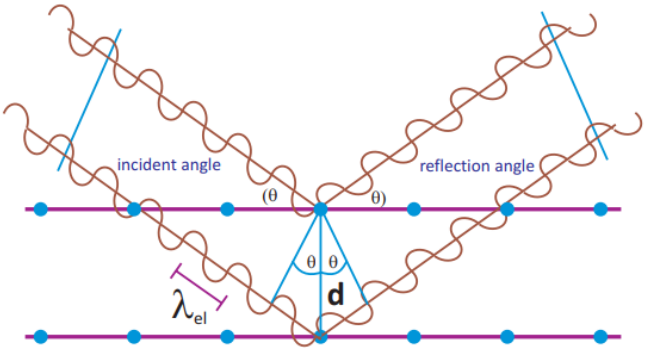

Figure 15:Bragg's law [91][92]

XRD diffractograms can also be used to figure out the grain size and lattice strain inside each unit cell. The intensity changes as the angle changes. Figure 16 shows how much information can be taken out. I_{max} and I_{int} can now be determined after background is removed (area under the peak). Several methods can be used to find the peak. Peak width can be determined by either half width at half maximum (FWHM), which is the peak width at half the peak intensity, or by integral breadth (IB), which is the breadth of a rectangle with the same peak intensity and mean intensity. It depends on what they are being used for to determine which peak parameter to use for measurements (Epp, 2016).

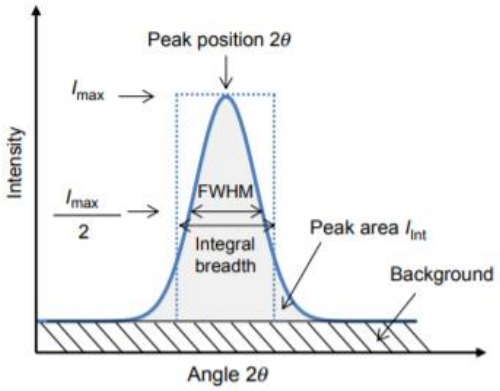

Figure 16:Diffraction peak [91]

As a method of determining grain size and strain, Warren-Averbach uses Fourier series of diffraction peaks. Cauchy and Gaussian functions were used to come up with equation 9(Bourniquel et al., 1989)

$$\frac{\beta_{hkl}^2}{\tan^2\theta} = \frac{\lambda}{D}\left(\frac{\beta_{hkl}}{\tan\theta \sin\theta}\right) + 25\langle\varepsilon^2\rangle \quad (9)$$

There are three things: D is the grain size, ε is the strain, and β_{hkl} the peak's breadth at half the intensity. Data points from peaks are linearly fitted onto $\left(\frac{\beta_{hkl}^2}{\tan^2\theta}\right)$ versus $\left(\frac{\beta_{hkl}}{\tan\theta \sin\theta}\right)$ as seen in Figure 17, the slope is a constant times strain value squared and the y-intercept is a constant divided by interplanar spacing.

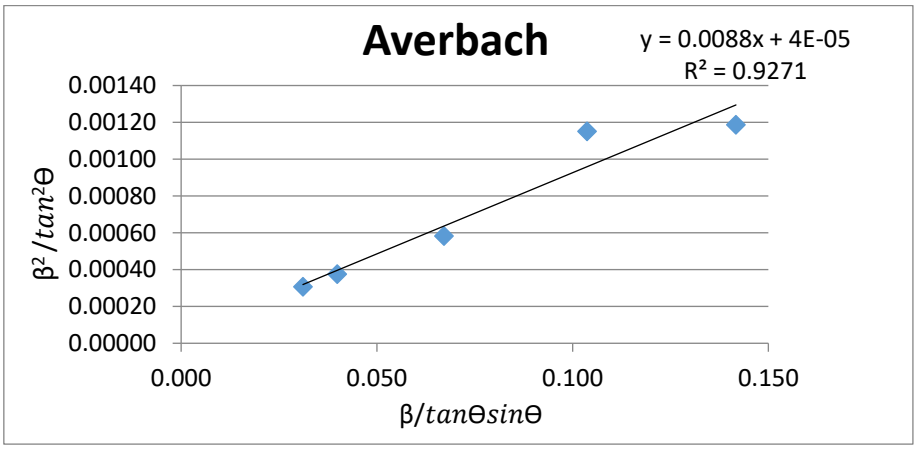

Figure 17:The Averbach plot for 0.1 SWCNTs/Bi0.4Sb1.6Te3

Scanning Electron Microscope (SEM):

An electron beam is used to create images of a material using scanning electron microscopy (SEM) in a voltage of 20 KV. (Figure 18). There are a wide range of signals generated by electron interactions with different atoms on the sample surface, providing information on the shape and composition of the sample surface. The SEM operates on the principle of scanning a specimen surface with a focused electron beam. The device is composed of four parts: a 2-inch thermal gun, a tungsten lamp, a microscope column, and a chamber for introducing samples. A beam of electrons traveling through a chamber under vacuum and emitted by a tungsten bulb scans the entire sample both vertically and horizontally. Images taken with a scanning electron microscope (SEM) are made possible due to secondary low-energy electrons (SEs) or backscattered electrons. The obtained images give information about the morphology of the samples.

Figure 18:SEM (FEI) at CLU, Qatar University

Transmission Electron Microscope (TEM)

One of the most often used techniques for studying materials, the transmission electron microscope (TEM) (shown in Figure 19) is used to study materials in a voltage of 200 KV and FEG emission of 60 µA. TEM analysis are used for extremely thin materials which have a high density of electrons in them. TEM need an electron gun, which produces the electron beam, as well as two other critical systems: one for creating the actual images and the other for recording them(*Transmission Electron Microscope | Instrument | Britannica*, n.d.). During the transmission of electrons, an image is created as a consequence of the interaction of electrons that are transmitted with and through the sample. Transmission electron microscopy (TEM) provides extensive information on the internal composition of the sample because of its high resolution. It may also be used to detect characteristics such as the crystal structure of the sample because of its high resolution(Pinto et al., 2018).Dark-field and bright-field images are the main end products of this technique. Only the direct beam interacts with the sample when the objective aperture is employed for the bright field image. In contrast, in a dark field image, the aperture stops the direct beam and enables only the diffracted beams to

pass through. The phase and amplitude of the beam determines the contrast of the resulting images, which is dependent on the kind and thickness of the sample. The electron population used to generate the TEM image is one of the fundamental differences between the bright field and dark field modes. The bright field image is the most typical image produced by a transmission electron microscope. Some portions of the sample may absorb or deflect electrons, resulting in a darker appearance, while others transmit electrons, resulting in a brighter appearance. In the bright field image, the aperture chooses the transmitted electron beam while blocking the scattered electrons. Due to the utilization of the unscattered beam, regions containing crystalline or high-mass materials will appear black. In dark field mode, the aperture rejects the unscattered electron beam and selects the scattered electrons instead. Therefore, areas without electron scattering (such as the area surrounding the sample) appear black, while places with materials appear brilliant. A bright field image can be boosted using this technique when it is not clear enough for imaging crystalline structures that are too small or obscured by background noise. Aside from that, it can be used to examine crystal lattices, crystal defects, stacking faults, dislocations, as well as particle/grain size (*TEM: Bright Field versus Dark Field - Chemistry LibreTexts*, n.d.).

Figure 19: TEM instrument,FEI at CLU, Qatar University

Raman Spectroscopy

Smekal proposed the phenomena of inelastic scattering of light in 1923 (Smekal, 1923), while Raman and Krishnan discovered it experimentally in 1928 (Raman & Krishnan, 1928). Raman spectroscopy (Figure 20.a) This phenomenon is known as the Raman scattering because it occurs when electrons and photons don't interact in the correct way. When a photon enters and a photon exits at different energies, Raman lines are generated. The emitted light's frequency causes Stokes lines to develop. It is termed "anti-stokes lines" if their frequency is lower than the photons that come into touch with them. The term "anti-stokes lines" refers to lines whose frequency exceeds that of the photons with which they come into contact. It is possible to identify the molecule present in a sample using the stokes and anti-stokes lines in the corresponding Raman spectra. If you look at the brightness of a sample, you can tell how concentrated it is has been used to describe the phenomena since then. A compound's distinctive Raman 'fingerprint' may be identified via Raman spectroscopy, which can provide chemical and structural information as well as identification. Through the detection of Raman scattering (Figure 20.b), Raman spectroscopy is used to extract this information from the material. Raman spectroscopy can tell you both about a substance's chemical and structural properties, as well as help you identify it by its unique Raman "fingerprint." Raman spectroscopy gets this information by looking for Raman scattering from the sample and then looking for that scattering. One of the things that Raman does is scattering. In this case, the oscillating electromagnetic field of a photon causes the molecular electron cloud to polarize. This causes the molecular electron cloud to become more or less polarized, leaving the molecule with more energy. If you think about it this way, the photon and molecule form a very short-lived complex. The "virtual state of the molecule" is what is referred to as the "virtual state of the molecule."

Because the virtual state is not stable in this scenario, the photon is re-emitted very immediately, in the form of scattered light, nearly immediately after it has been emitted. It occurs once per 10 million photons, which is very rare. This is referred to as Raman scattering, which is an inelastic scattering mechanism that results in a transfer of energy between the molecule and the photon that was emitted from it. During Stokes Raman scattering, the molecule receives more energy from the photon than during other types of scattering. As a result, the photon loses energy and the wavelength of the photon increases in length (after G. G. Stokes). Anti-Stokes Raman scattering is a kind of Raman scattering that uses anti-Stokes Raman scattering. It is known as Anti-Stokes scattering when a molecule loses energy as a result of relaxing to a lower vibrational state, and the scattered photon acquires the same amount of energy as the molecule while having a shorter wavelength. According to quantum physics, both Stokes and Anti-Stokes effects are feasible. The Boltzmann distribution indicates that the majority of molecules are at the ground vibrational level when there are a large number of molecules, and Stokes scatter is the more probable process when there are a large number of molecules. As a consequence, the Stokes Raman scatter is always more intense than the anti-Stokes Raman scatter, regardless of the situation. In Raman spectroscopy, it is for this reason that the Stokes Raman scatter is virtually always seen. This phenomenon is known as the Raman scattering because it occurs when electrons and photons don't interact in the correct way. When a photon enters and a photon exits at different energies, Raman lines are generated. The emitted light's frequency causes Stokes lines to develop. It is termed "anti-stokes lines" if their frequency is lower than the photons that come into touch with them. The term "anti-stokes lines" refers to lines whose frequency exceeds that of the photons with which they come into contact. It is possible to identify the molecule present in a sample using the stokes and anti-stokes

lines in the corresponding Raman spectra. If you look at the brightness of a sample, you can tell how concentrated it is(E. Smith & Dent, n.d.).

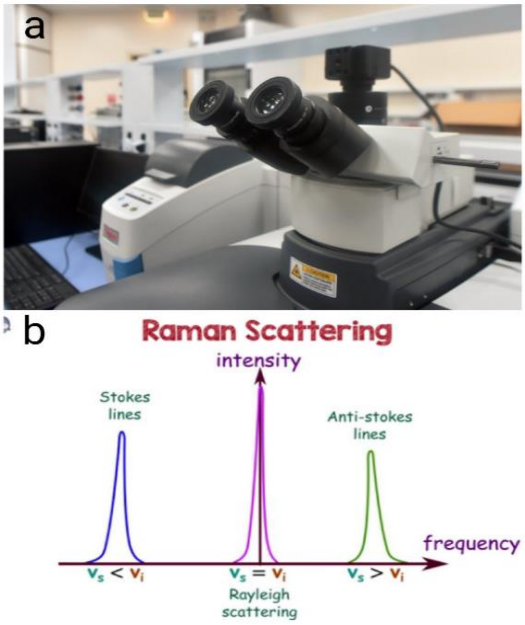

Figure 20:a) Raman spectroscopy (Raman Thermo Scientific DXR3)at CLU, Qatar university, b) Types of Raman scattering [101]

Mechanical Properties Characterization

Vickers Hardness (HV)

As the name suggests, Vickers hardness testing(future-tech,FM,ARS 9000) (Figure 21, equation 10) is the method of hardness testing that employs a micro indentation technique, otherwise known as the 136 degree diamond pyramid test. Using the indenter, a square indentation is created along the diagonal. (Deepa et al., 2019).

$$HV = \frac{F}{A} \cong 1.854 \frac{F}{d^2} \qquad [\mathrm{kgf/mm^2}] \qquad (10)$$

In determining hardness, the fundamental principles are the same for all measures, which are a material's resistance to plastic deformation when measured from a standard source. A square trapezium diamond is used in an indentor to create indentions on the surface of a material using a certain amount of force and time. Among all hardness tests

available, the Vickers hardness test is most comprehensive, meaning that it can be used on all metals. The Vickers Pyramid Number (HV), also known as Diamond Pyramid Hardness, is a measurement of hardness that is measured using the Vickers Pyramid Test. Despite the fact that the hardness value may be converted to pascals, it should not be confused with pressure, which uses the same units. The load applied to the indentation's surface area, not the area corresponding to the force, determines the hardness number, which is not pressure. (R. L. Smith & Sandland, 1922) The conditions used during measuring the hardness were that the holding time was 5 seconds and the load was equal to 25 gf.

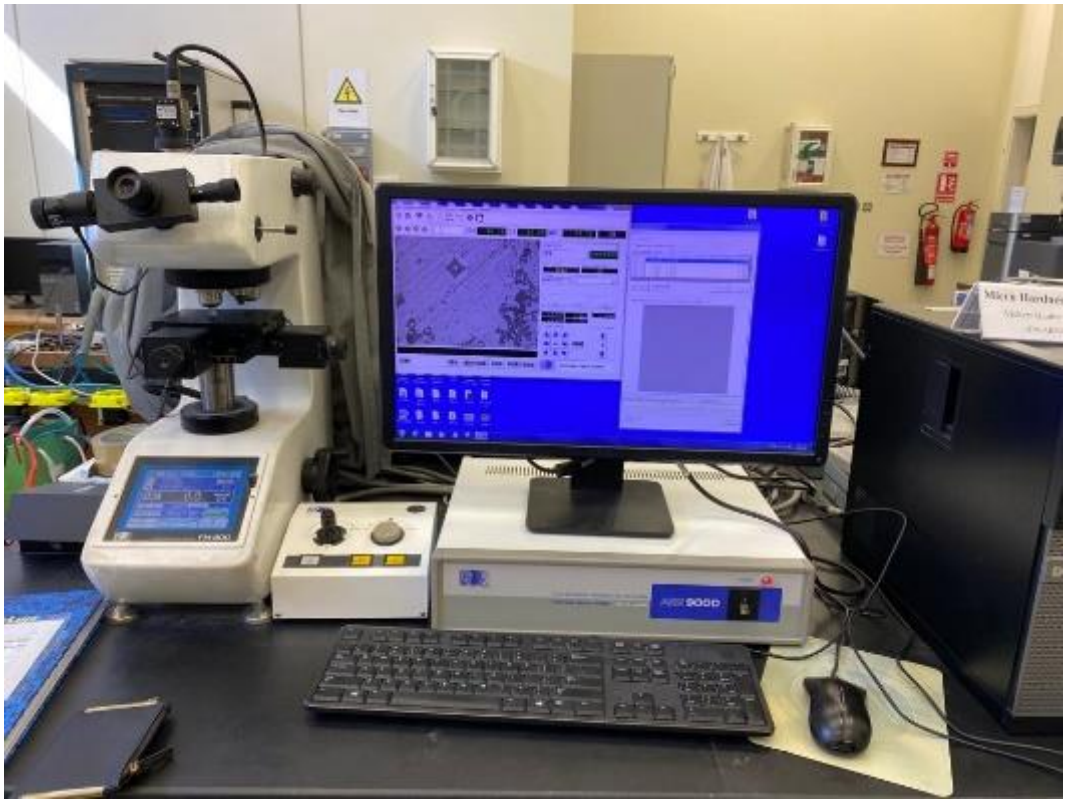

Figure 21:Vickers' Hardness instrument (Future-Tech) at CAM, Qatar University

THERMOELECTRIC PROPERTIES CHARACTERIZATION:

Seebeck coefficient and the electrical conductivity

Different instruments are available for measuring the Seebeck coefficient or electrical conductivity, but their operating principles are different. This study utilized the

NETZSCH 'SBA 485 Nemesis (Figure 22) with 3.5 Volts and 0.4 A current. This instrument utilises a four-point system. SBA 485 Nemesis instrument structures the sample between two micro heaters, thermocouples, and current pins. The Seebeck coefficient is tested using microheaters that generate cyclic heating by alternately generating a temperature gradient. A voltage is produced between the two thermocouples as a result of this temperature differential. By plotting the measured voltage versus temperature difference, the Seebeck coefficient can be calculated. As well as measuring electrical conductivity, the same device is used to measure voltage between its two ends after applying various currents to the two current pins.

Figure 22:Electrical conductivity SBA setup(Nemesis), Qatar University

Thermal conductivity

Thermal conductivity is a feature of a material that defines the temperature ranges at which it may be used. (Peng et al., 2020) In general, the thermal conductivity of a material is the rate at which heat moves through a given area of that material. Heat transfer rates are generally proportional to thermal conductivity, with greater thermal conductivity resulting in faster heat transfer rates and vice versa(Oladijo et al., 2021). It is often represented by the letter 'k,' however it may also be represented by the symbols " λ". Thermal resistance is the inverse of this quantity. Thermoelectric

materials with high thermal conductivity are utilized in heat sinks, while thermal insulators are made of materials with low levels of thermal conductivity. Fourier's law of thermal conduction (equation 11), (alternatively called the law of heat conduction) says that the rate at which heat is transported through a material is proportional to the area over which heat flows and the temperature gradient. The differential version of this law is given as follows:(*Thermal Conductivity | Open Science Wiki | Fandom*, n.d.)

$$q = -k.\nabla T \quad (11)$$

Where ∇T indicates the temperature gradient, q means the thermal flow or heat flux, and k defines the material's thermal conductivity(*Thermal Conductivity | Open Science Wiki | Fandom*, n.d.). The Thermal conductivity apparatus used was (C-Therm) and the measurement technique was MTPS(Modified Transient Plane Source Method)(Figure 23).

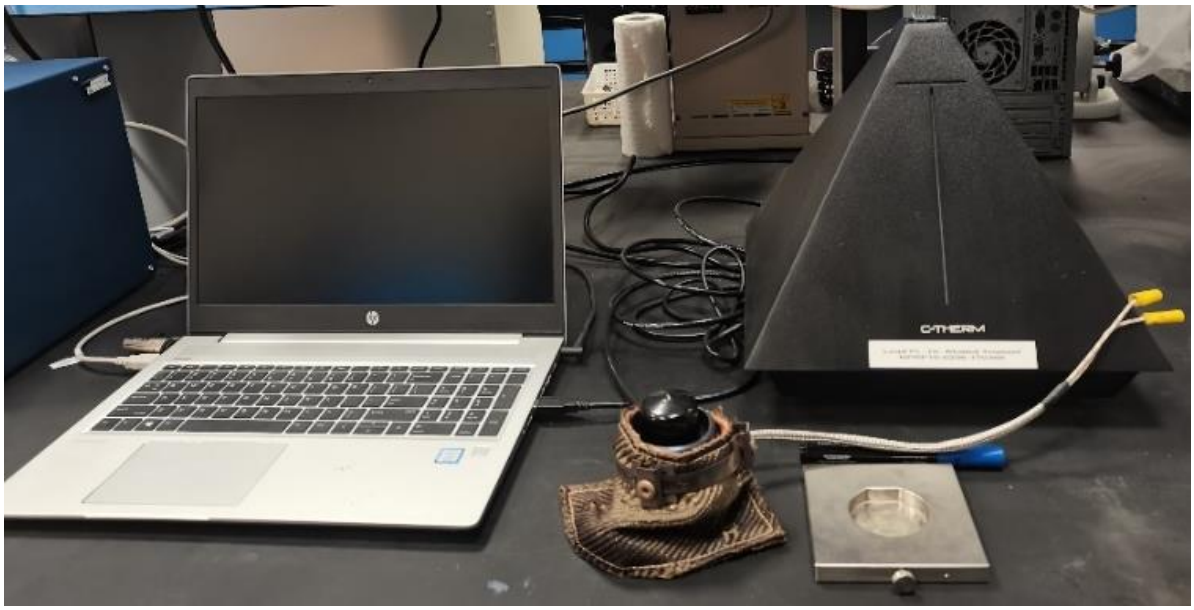

Figure 23:The thermal conductivity setup (C-Therm),Qatar University

CHAPTER 4: RESULTS & DISCUSSION

Prepared SWCNTs/ $Bi_{0.4}Sb_{1.6}Te_3$ Composites

Ball milling technique was used to grind the samples to be in the nanoscale size and then by use of X-ray diffraction, the crystallinity of the samples was analysed (XRD). Figure 24.a shows the XRD analysis for the powder of SWCNTs/ $Bi_{0.4}Sb_{1.6}Te_3$ different composites. Figure 24.b shows the XRD analysis for the same composites after disc formation in the Hot Press setup. All the peaks in Figure. 24 match the reference code 00-049-1713 of $Bi_{0.4}Sb_{1.6}Te_3$. As shown in Figures 24a,b all the peaks were similar to the pristine composition of $Bi_{0.4}Sb_{1.6}Te_3$ and match with the XRD shown in literature (Ahmad et al., 2016a). Thus, there are no peaks were shown for SWCNTs as they were added in small amounts. All powders were polycrystalline and has a rhombohedral structure (space group R3m) (Kadhim et al., 2013). Grain size was calculated using XRD peaks (Table 2) and showed better fitting and high regression values for Warren-Averbach model. Since all samples were exposed to the same milling time (16 hrs), therefore all samples were expected to have the same average grain size 17 nm according to Warren-Averbach calculations. The resulting XRD was comparable to the reported XRD in another study published in the literature(Ahmad et al., 2016a).While the previous study and this existing study used different ball milling processes. For this present work, ball milling for 16 hours was performed on $Bi_{0.4}Sb_{1.6}Te_3$ compositions combined with SWCNTs and pure $Bi_{0.4}Sb_{1.6}Te_3$ compositions (without the addition of SWCNTs). In contrast, the previous comparison study showed that p-type bismuth telluride compositions were ball milled for 24 hours. The resulting BiSbTe particles were then stirred in ethanol for 30 minutes. (Ahmad et al., 2016a) And SWCNTs were mixed into ethanol for ultrasonication for 30 minutes. The slurry of BiSbTe and SWCNTs was then combined and ultrasonically mixed with a magnetic stirrer for 30

minutes. Finally, the dispersed slurry of BiSbTe and SWCNTs in ethanol was ball-milled for 2 hours to protect SWCNTs(Ahmad et al., 2016a).

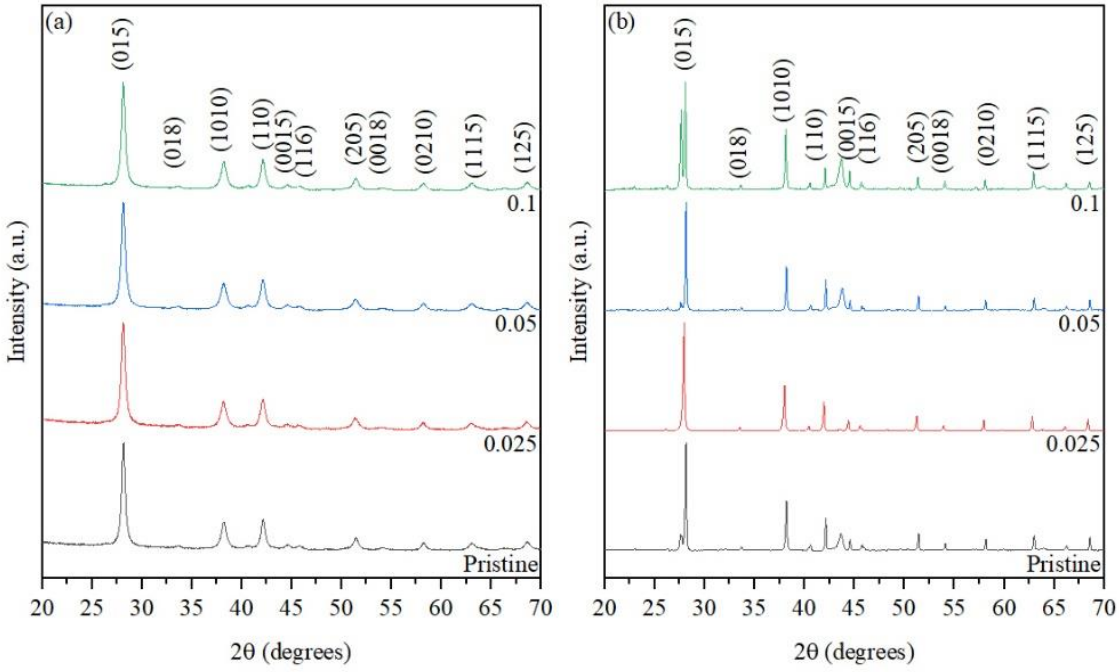

Figure 24: XRD analysis of SWCNTs/ Bi0.4Sb1.6Te3 composites: a) for as milled powder form, b) for disc form (after consolidation)

Table 2:Grain size calculations according to XRD Figure, R^2 and strain calculations

Composition	**Grain Size (nm)**	**R^2**	**Strain**
0 SWCNTs	18	0.92	0.140
0.025 SWCNTs	17	0.92	0.165
0.05 SWCNTs	16	0.91	0.141
0.1 SWCNTs	17	0.92	0.133

Furthermore, Figure 25 shows how the Vickers hardness indentation method was used to find the hardness of each of the four mixtures. Figure 25 shows that 0.1 wt. % of SWCNTs/$Bi_{0.4}Sb_{1.6}Te_3$ had the highest hardness, which was 1.34±0.01 Gpa, while 0.025 wt. % had the lowest hardness, which was 1.15±0.01 Gpa. And our hardness data

is showing better values than the reported value for bismuth telluride at room temperature which equals to 0.62 Gpa as reported in literature(Zheng et al., 2020).This result backs up what Bahadar et al. (2020) said about how adding SWCNTs makes Nano composites harder(Bahadar & Zwawi, 2020). In this study, adding SWCNTs made the material harder. This is because the interaction between SWCNTs and composites leads to mechanical interlocking, which makes it easy for loads to be transferred between the composites and nanotubes(Bahadar & Zwawi, 2020). The overlap and stacking of bismuth telluride components, which boosts the material's resistance to scratching and plastic deformation, is another reason why the addition of SWCNTs nanofiller boosted the composites' hardness(Mekdad et al., 2020).

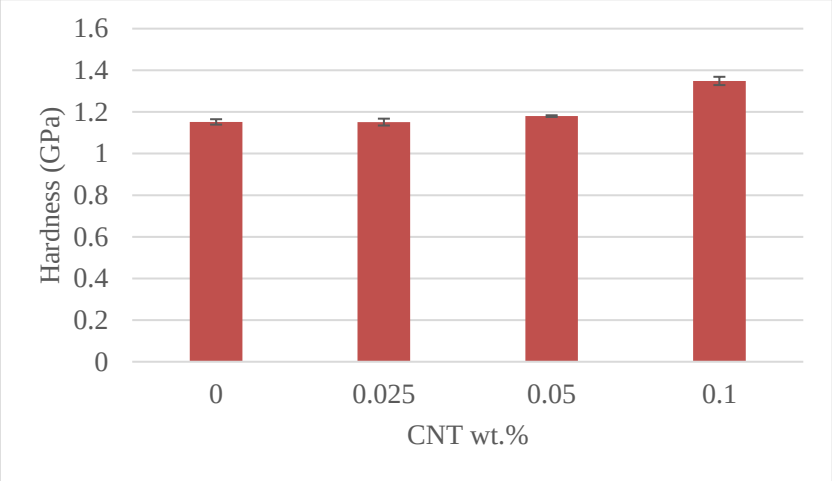

Figure 25: Hardness data for SWCNTs/ Bi0.4Sb1.6Te3 compositions after formation of discs

The shape of SWCNTs is shown in Figure 26. The surface morphology of the composites may be determined from the SEM data displayed in Figures 27.a, 28, and all samples exhibited nanoparticle agglomeration. Due to the high specific area (surface area to volume ratio) of particles, agglomeration is widespread in nanomaterials, resulting in a shift in the dominant forces acting on the material(Agrawal & Rai, 2015). Consequently, the existing weak Van der Waals forces have a higher influence on the

nanoscale than they do on equivalent bulk materials, causing agglomeration(Du et al., 2019). Although there are a large amounts of SWCNTs were added to composition $Bi_{0.4}Sb_{1.6}Te_3$, the SEM analysis is showing only the agglomeration of nanoparticles. SEM mapping analysis was run to prove the presence of SWCNTs in the compositions other than the pristine as shown in Figure 27, 28 respectively. Bi, Te, Sb, and C are distributed uniformly across the sample, also as seen in Figures 27, 28.

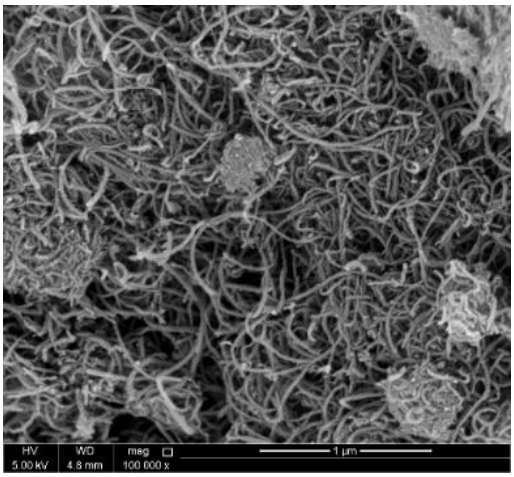

Figure 26: represent the shape of SWCNTs under the SEM

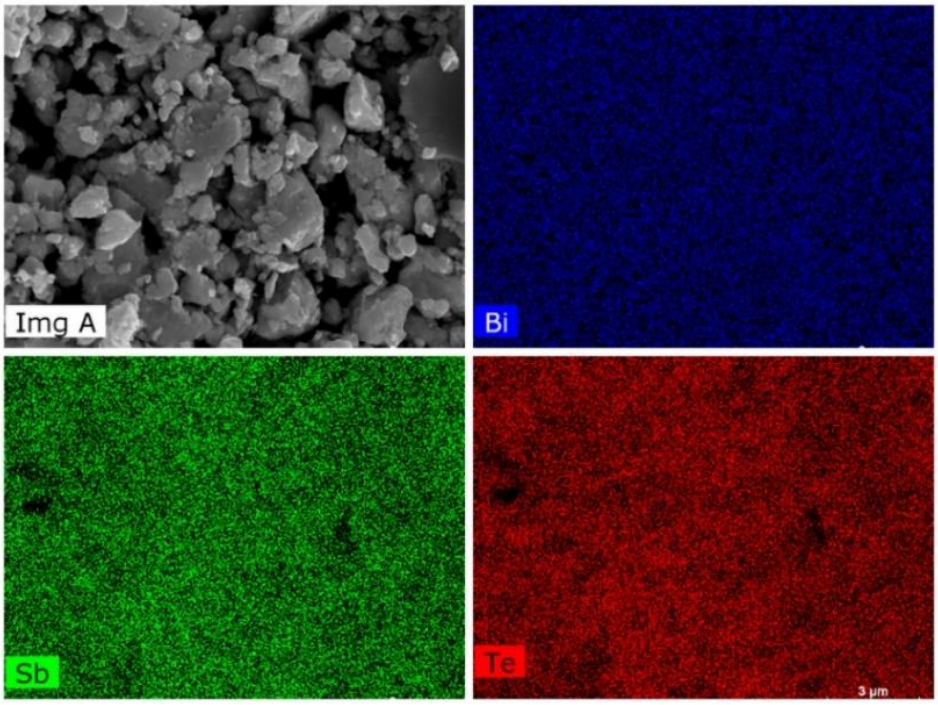

Figure 27:The SEM elemental mapping for 0 wt. %of SWCNTs/Bi0.4Sb1.6Te3

Composition.

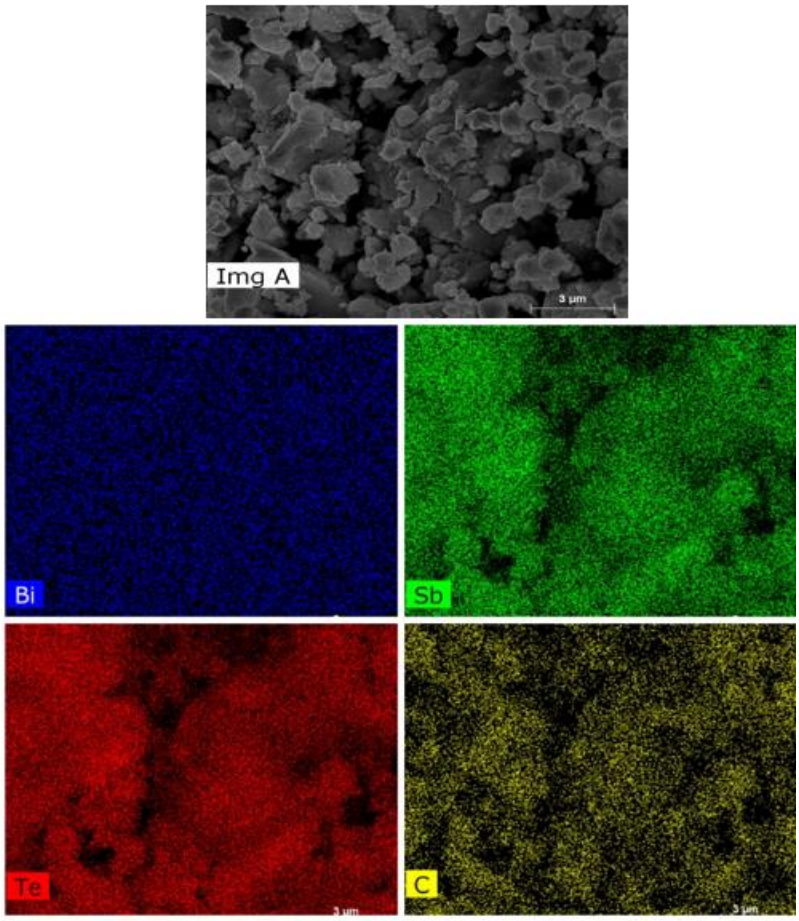

Figure 28: The SEM elemental mapping for 0.025 wt.% of SWCNTs/Bi0.4Sb1.6Te3 composition

The degree of crystallinity and structural defects of SWCNTs were investigated using Raman spectroscopy and the results are shown in Figure 29. The Raman spectra of produced SWCNTs/$Bi_{0.4}Sb_{1.6}Te_3$ nanocomposites show three distinct bands. The first is the D band, which represents the degree of defect in the carbon lattice. The defect induced D-band, which is detected at 1300 - 1400 cm^{-1}, is the most studied mode for the characterisation of functionalized SWCNTs. The D-band intensity is the most researched property in functionalized SWCNTs. Because the development of the D-peak is caused by defects, a rise in D-band intensity is used as a fingerprint for successful functionalization (Ouyang et al., 2008). The second and third bands are SWCNTs' signature bands, the G and 2D bands. The tangential modes are the most

intense high-energy modes of SWCNTs and represent the so-called G-band, which is commonly detected at a wavelength of roughly 1600 cm^{-1} (Suzuki & Hibino, 2011).The G′-band (also referred to as the D*-band or 2D-band) seen at 2600 - 2800 cm^{-1} does not need defect scattering (Graupner, 2007; Suzuki & Hibino, 2011). This also establishes a clear link between the structural integrity of SWCNTs and its milling time. Table 3 displays the range of Raman shift values for the samples, which is comparable to those of previous studies of SWCNTs Raman spectra (Kaleńczuk et al., 2008). In Raman spectra of CNTs research, relative Raman intensities (I_D/I_G) are often utilized to quantify defect concentration and impurities (Wang et al., 2009),(Ouyang et al., 2008). A low I_D/I_G ratio indicates a low defect concentration in CNTs. The I_D/I_G represents the crystal structural integrity of SWCNTs (Ouyang et al., 2008). As seen from the table, the higher the amount of SWCNTs, the more value of I_D/I_G. The increase in the I_D/I_G ratio indicates that composites containing a higher concentration of SWCNTs have a greater number of structural defects than composites containing a lower concentration of SWCNTs (S. Singh et al., 2020). The calculated intensity ratio of I_D/I_G for SWCNTs in the composite samples is high and greater than 1 (compared to 0.3 for as received SWCNTs) since all composites were prepared in the same milling time (Wang et al., 2009).

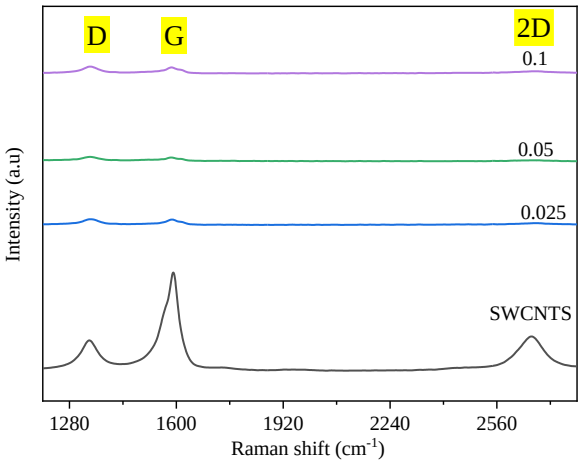

Figure 29: Raman analysis for Bi0.4Sb1.6Te3 compositions and SWCNTs

Table 3: Raman Shift for SWCNTs in D and G Bands, and I_D/I_G Ratios of the Prepared Composites

Intensity	**as received SWCNTs**	**0.025**	**0.05**	**0.1**
I_D	245.6031	30.16411	46.74926	52.53711
I_G	796.966	25.13232	43.31131	46.05198
I_D/I_G	0.308173	1.200212	1.079378	1.140822

Figure 30 shows the nano structure of SWCNTs under TEM. TEM analysis were carried on for this study and dark field image (Figure 31.a) was used to calculate the grain size to compare it with that obtained from XRD calculations. Image J software was used to measure the size of grains in the dark field image Figure 31a. The dark-field (DF) TEM micrographs of the $Bi_{0.4}Sb_{1.6}Te_3$ matrix demonstrate homogeneous grain sizes and distribution without the presence of significant agglomerated nanocrystallites, as illustrated in Figure 31.a. Figure 31.b shows a BF-TEM micrograph of the $Bi_{0.4}Sb_{1.6}Te_3$ matrix with equiaxed and randomly dispersed grains inside the nanocomposite structure. Figure 31.c shows the atomic planes of the pseudo hexagonal $Bi_{0.4}Sb_{1.6}Te_3$ nano grains, which corresponds well with the XRD patterns. Figure 31.c shows the diffraction pattern which seem to be equiaxed in random orientations that fit their diffraction characteristic in the XRD patterns Figure 31c(Lemine et al., 2022). As shown in Figure 31.d, the average grain size is 15±6 nm, which is slightly lesser than the calculated grain size from XRD using the Warren Averbach model of 17 nm, but within the range of uncertainty.

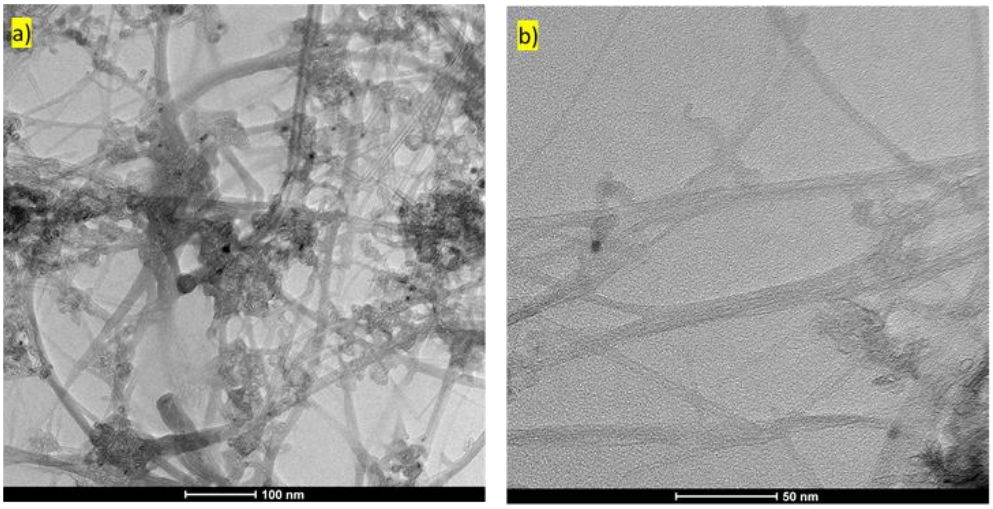

Figure 30:bright field TEM of SWCNTs, a) at 100 nm scale, b) at 50 nm scale

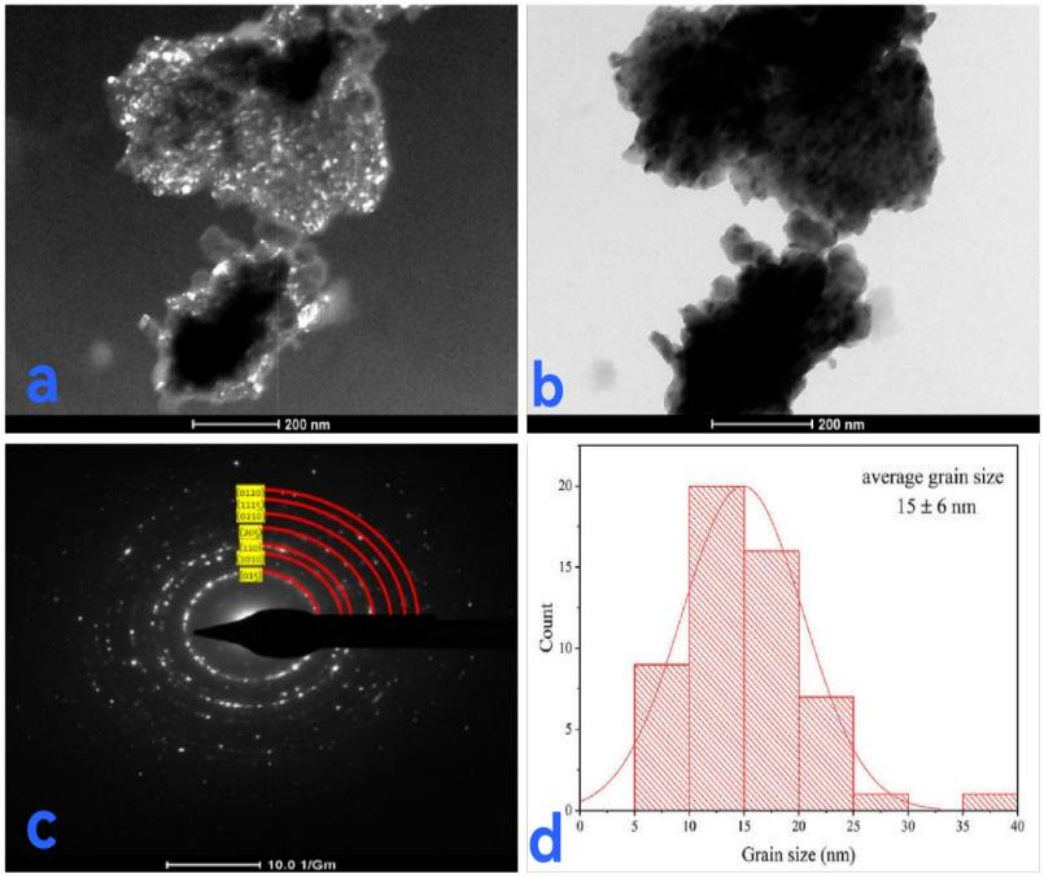

Figure 31: TEM analysis for as milled powders of 0.1 wt. % SWCNTs/ Bi0.4Sb1.6Te3 Composites: a, b) dark field and bright field of respectively, c) diffraction pattern of Bi0.4Sb1.6Te3 (0 wt.% SWCNTs), d) Grain size distribution for 0.1 wt.%.

Thermoelectric Properties of SWCNTs/ $Bi_{0.4}Sb_{1.6}Te_3$ Discs

SWCNTs-based bismuth telluride composites and the pristine sample are compared and analyzed in terms of electrical conductivity, Seebeck coefficient, and thermal conductivity. These findings have also been used to calculate and evaluate the power factor and figure of merit. Due to their near-room-temperature application, these alloys are used for high-temperature applications, all SBA property findings were analysed from room temperature to 300 degrees of Celsius, and thermal conductivity was analysed from room temperature to 150 degrees Celsius(Neeli et al., 2016).

Electrical Conductivity

The trends of compact discs' electrical conductivity are shown in Figure 32. All of the samples behaved like degenerate semiconductors because their electrical conductivity dropped as the temperature increased. This was similar to what other SWCNTs-based studies on p-type bismuth telluride found(Ahmad et al., 2016a).In general, the electrical conductivity of all samples exhibits semi-metallic conductivity behaviour, decreasing with increasing temperature (Figure 32). Incorporating SWCNTs networks into the matrix has an impact on the electronic transport, according to the nonlinear behaviour of electrical conductivity for SWCNTs/ $Bi_{0.4}Sb_{1.6}Te_3$ composites in the temperature range of 175 ℃ to 300 ℃. Typically, SWCNTs comprise a combination of semiconducting and metallic nanotubes, with semiconducting nanotubes being the majority. Since a thin network of semiconducting nanotubes predominates the electronic transport in the composites, it may be concluded from the nonlinear behaviour, namely the rise in slope of electrical conductivity with the addition of SWCNTs in $Bi_{0.4}Sb_{1.6}Te_3$ at temperature 250℃. Moreover, because SWCNTs is smaller than the bismuth telluride nano grains and electrons have to travel through the nanotubes so it takes longer path for the electron to travel through the nanotubes than

the direct path through the bismuth telluride grains. Therefore, this longer path length decreases the electrical conductivity. Aonother reason could be the reason of low electrical conductivity is the tunnelling resistance due to poor electrical contacts(El-Makaty et al., 2021). The addition of 0.025 by weight of SWCNTs reduces the electrical conductivity of the $Bi_{0.4}Sb_{1.6}Te_3$ composite compared to that of 0 wt. % SWCNTs/ $Bi_{0.4}Sb_{1.6}Te_3$. Additional additions at 0.05 wt.% and 0.1 wt.% enhanced the composites' electrical conductivity gradually(Ahmad et al., 2016b).

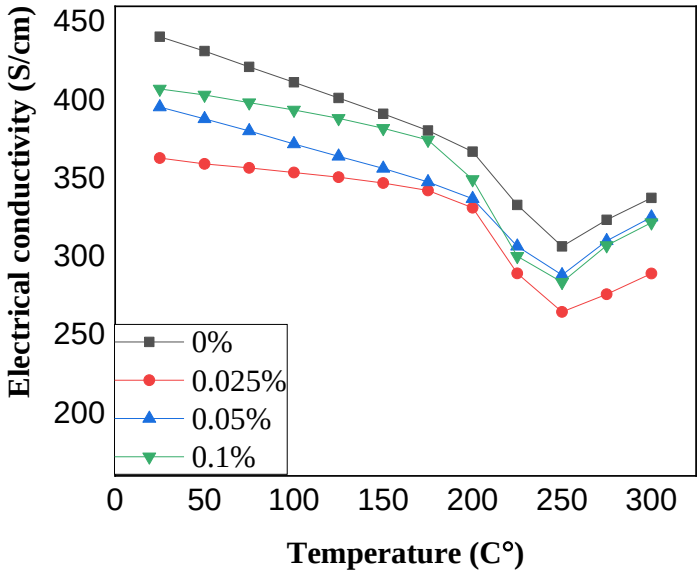

Figure 32:Electrical conductivity trends for SWCNTs/ Bi0.4Sb1.6Te3 Samples

Seebeck Coefficient

The temperature dependency of a composite's positive Seebeck coefficient is shown in Figure 33, suggesting that all samples are p-type. At 175 degrees Celsius, the greatest Seebeck coefficient of 197.9 uV/K is measured for 0.05 weight percent SWCNTs/ $Bi_{0.4}Sb_{1.6}Te_3$ composite. It reduced to 186.8 uV/K at the same temperature with 0.05 weight of SWCNTs, showing that the higher carrier density is consistent with earlier findings(Ahmad et al., 2016a). The Seebeck coefficient increases and decreases whereas electrical conductivity decreases and increases across the entire temperature

range. This tendency might be partially explained by a reduction in carrier mobility carried on by increased scattering at grain boundaries and SWCNTs/matrix interfaces. The conductive nature of SWCNTs is mainly responsible for the decrease in Seebeck coefficient when trend decreases from 0.05 wt.% percent to 0.1 wt. percent and 0.025 wt.% percent. The Seebeck coefficients first increase with temperature, peak, and then decrease. Previous research has suggested that this phenomena may be connected to the thermal excitation of minority carriers(Ahmad et al., 2016b).

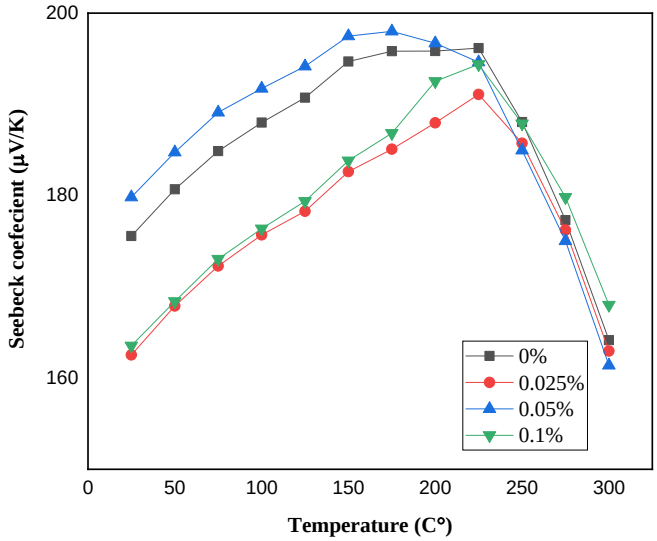

Figure 33:Seebeck Coefficient trends for SWCNTs/ Bi0.4Sb1.6Te3 Samples

Power Factor

Figure 34 displays the variation in power factor with temperature for all composites. Between 25 and 150 ̊C, the power factor achieves its peak values; after that, it decreases as temperature increases. The power factor decreases when SWCNTs are added, in contrast to the Seekbeck coefficient, which often rises. The decline in electrical conductivity behaviour is mainly to answer for the drop in power factor for SWCNTs/BiSbTe composites. As a result, the behaviour of the power factor is dominated by electrical resistivity(Ahmad et al., 2016b).

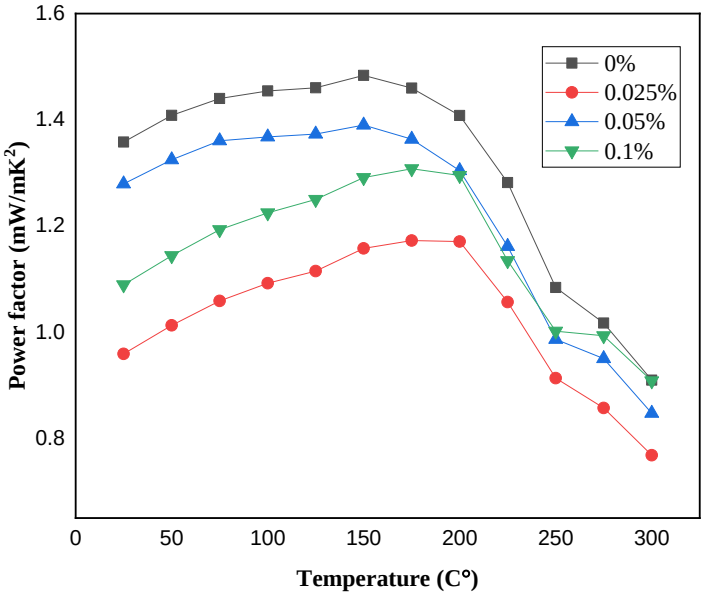

Figure 34: Power factor trends for SWCNTs/ Bi0.4Sb1.6Te3 Samples

Thermal conductivity

Figure 35 shows the thermal conductivity trends for the SWCNTs/ $Bi_{0.4}Sb_{1.6}Te_3$ samples as well as the pristine sample. According to the data collected, the highest thermal conductivity trend was the pristine (0 wt. % SWCNTs) behavior and this means that the SWCNTs addition reduced the thermal conductivity of the SWCNTs/composites when compared to the behavior of 0 wt. % of SWCNTs composites, as shown in Figure 35. Furthermore, when the temperature rises from 30 degrees Celsius to 80 degrees Celsius, the addition of SWCNTs increases the thermal conductivity trends. As a result, in order to better understand the impact of total thermal conductivity, the electronic and lattice components were determined using equations (12) and (13), and their graphs are given in Figures 36, 37.

$$k_E = \sigma T L \tag{12}$$

$$k_{\text{Total}} = k_E + k_L = D\rho C_p \tag{13}$$

The lattice conductivity trends were reduced for all the samples. The electronic thermal conductivity trends show that increasing the amount of SWCNTs increased the trends of electronic thermal conductivity for the SWCNTs/composites and even the pristine one as explained in Figure 37. As explained in literature the increasing of SWCNTs weight in the BiSbTe composite increases the thermal conductivity and decreasing the weight of the SWCNTs by 0.05 and 0.025 will decrease the thermal conductivity trends(Ahmad et al., 2016c). The addition of SWCNTs at higher weights equal to 0.1 wt. % reduced the lattice thermal conductivity as compared to the pristine sample, 0.025% and 0.05% samples as seen in Figure 36. As explained in literature by Ahmed and Nabi ,2017 at two different publications that the decrease in lattice thermal conductivity as the amount of SWCNTs increase is mostly due to phonon scattering at the nanotubes and BiSbTe nanostructure boundaries (Ahmad & Wan, 2017; Nabi et al., n.d.). This approach is beneficial in the applications of thermoelectric materials since it does not change the electrical component of thermal conductivity and thus has a little impact on the electrical transport properties. According to studies, nanostructuring affects the lattice conductivity as compared to the electronic transport characteristics(Nabi et al., n.d.). The Wiedemann–Franz law may be used to determine the electronic thermal conductivity using the relation $K_e = LT/R$, where T is the absolute temperature, R is the electrical resistivity, and L is the Lorenz number. As seen in Figure37 the electronic thermal conductivity show an inverse proportional relationship at temperature range of 30-150 C. And it is seen in Figure 37 that adding smaller weight of SWCNTs to the composite contribute in reducing the electronic thermal conductivity. Therefore, it can be concluded that thermal conductivity was effectively restrained by the inclusions of Single walled carbon nanotubes and defects by SWCNTs(Y. Zhang et al., 2012).

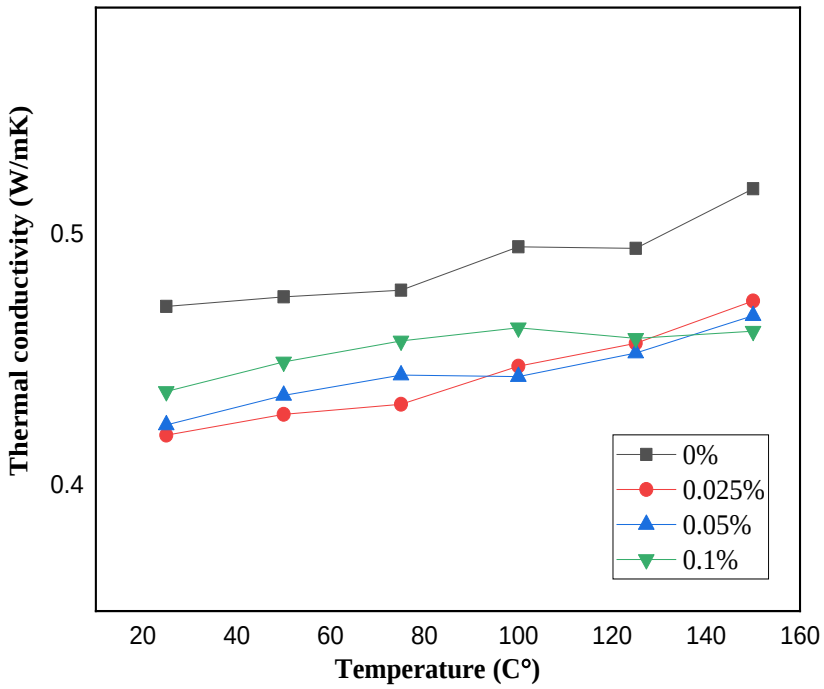

Figure 35: Thermal conductivity trends for SWCNTs/ Bi0.4Sb1.6Te3 Sample

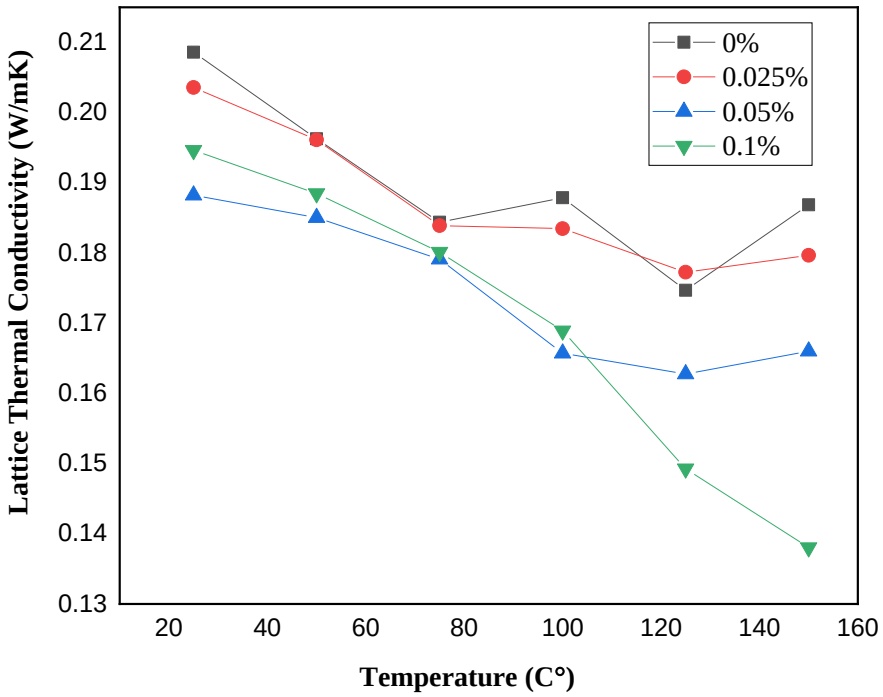

Figure 36: Lattice Thermal conductivity trends for SWCNTs/ Bi0.4Sb1.6Te Sample

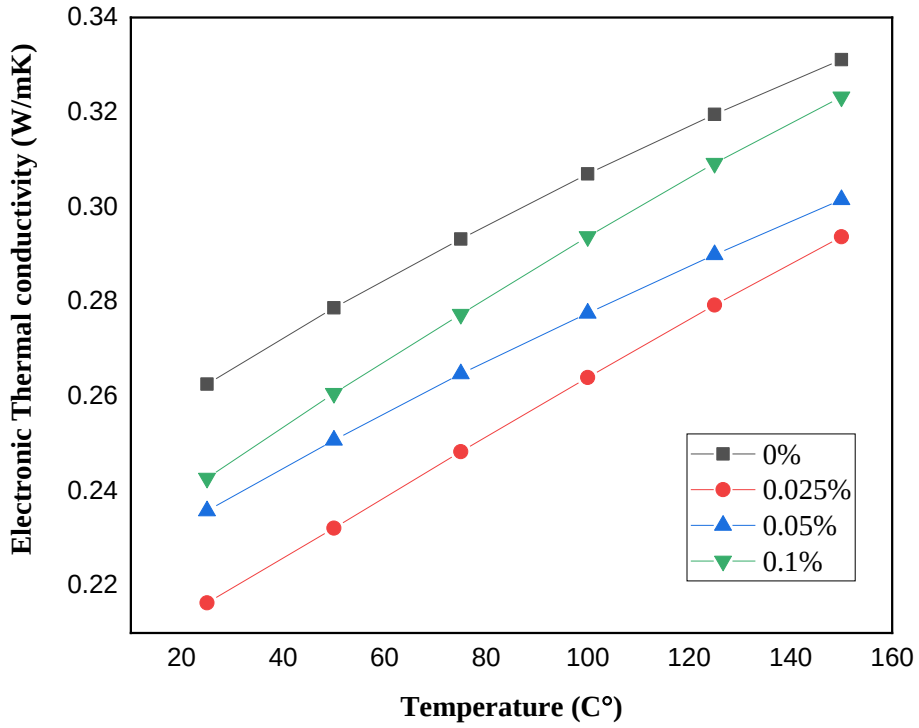

Figure 37:Electronic thermal conductivity trends for SWCNTs/ Bi0.4Sb1.6Te3 Samples

The figure of Merit

As explained in literature, the figure of merit is increased for the p-type bismuth telluride composites with SWCNTs less than 0.5(Ahmad et al., 2016c). The figure of merit was enhanced within the 0.05 composite by obtaining the highest ZT value equal to 1.26 at 150 ̊C as seen in Figure 38. And this followed by the pristine sample, 0.1 wt.% composite and finally 0.025 wt.% respectively. As compared to 0.1 wt. percent and 0.025 wt. % percent SWCNTs/BiSbTe composites, the reduction in thermal conductivity of 0.05 wt. % percent produces a considerably greater figure of merit. Besides reduction obtained in thermal conductivity, the reduction in electronic thermal conductivity as well for the 0.05% in Figure37 is the reason that ZT had highest trend for 0.05%(Lognoné & Gascoin, 2014). In contrast to the pristine sample (0.05%), the

addition of SWCNTs at room temperature increased ZT by 5% from 0.86 to 0.90 when compared to the optimum sample (0.05%). For the same sample, ZT increased from 1.21 to 1.26 at 150 ◦C, resulting in a total improvement of 4%. As Ahmed et al (2017) indicate, these findings demonstrate strong overall improvements when adding SWCNTs in percentages below 0.5 to existing SWCNTs/Bi2SbTe3 samples. The maximum ZT values obtained by Ahmed et al[120]. at 147 ℃ and room temperature were 0.7 and 0.48 respectively(Ahmad et al., 2016c).This High ZT we obtained in our study is because that CNT act as a thermal barrier due to the formation of large interfaces in the matrix as reported in literature(K. T. Kim et al., 2013a).

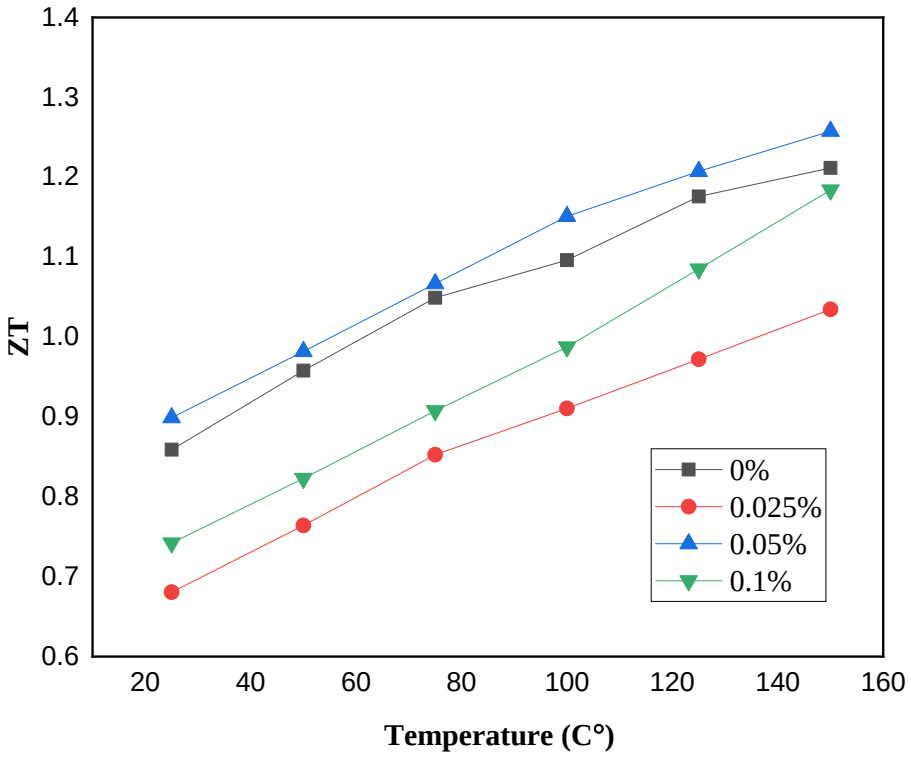

Figure 38:Variation of ZT versus temperature

CHAPTER 5: CONCLUSION

In conclusion, through ball milling technique, a nanocomposite of SWCNTs and bismuth telluride was successfully prepared. Thermal properties of powders were measured after they were compacted using the HotPress Setup.

- The nanostructured p-type material was milled for 16 hours.
- The average grain size of the powders that were created as milled powders was 17 nm calculated by Averbach method and grain size of 15 ± 6 nm obtained by TEM grain size calculations.
- Hardness values for the SWCNTs composites showed highest hardness for 0.1 wt.% of SWCNTs concentration which equals to 1.34±0.01, and lowest hardness for 0.025 wt.% which equals to 1.15±0.01, this demonstrates the capacity of SWCNTs to adjust the hardness of the samples as compared to the original sample.
- The calculated intensity ratio of I_D/I_G for SWCNTs in the composite samples is high and greater than 1 (compared to 0.3 for as received SWCNTs) since all composites were prepared in the same milling time (Wang et al., 2009)Electrical conductivity trends showed that the addition of 0.025 by weight of SWCNTs reduces the electrical conductivity of the $Bi_{0.4}Sb_{1.6}Te_3$ composite compared to that of 0 wt.% of SWCNTs/ $Bi_{0.4}Sb_{1.6}Te_3$. It is noticed that 0.05 wt.% and 0.1 wt.% enhance the composites' electrical conductivity gradually.
- Seebeck coefficient values were enhanced only for the sample which contain 0.05 weights of SWCNTs.
- The power factor value indicated that the optimum sample has 0.05 weight percent of SWCNTs.

- SWCNTs addition reduced the thermal conductivity of the SWCNTs/composites when compared to the behavior of 0 wt. % of SWCNTs composites.
- The addition of SWCNTs had increased ZT at room temperature from 0.86 to 0.90 for the optimum sample (0.05) by 5%. Whereas at the optimum temperature of 150 ºC, ZT had a total improvement of 4% reaching a value of 1.26, for the same sample.

The ZT enhancement may be caused by nanostructuring and the presence of 1D SWCNTs nanofiller. Continues work should be done to achieve better ZT results through tailoring the percentages of SWCNTs and the ratio of bismuth telluride to p-type and n-type materials.

Table 4:Acronym List:

Acronym	Definition
SWCNTs	Single walled carbon Nano tubes
TE	Thermoelectric materials
SEM	Scanning electron microscope
TEM	Transmission electron microscope
ZT	Figure of Merit
XRD	X-ray Diffraction
Wt.	Weight

REFERENCES:

A. F. Ioffe Semiconductor Thermoelements And Thermoelectric Cooling Infosearch (1957) : Free Download, Borrow, and Streaming : Internet Archive. (n.d.). Retrieved October 1, 2021, from https://archive.org/details/A.F.IoffeSemiconductorThermoelementsAndThermoelectricCoolingInfosearch1957

Agrawal, S., & Rai, M. (2015). Performance analysis of multi walled carbon nanotube (MWCNT) bundle as VLSI interconnects. *Undefined*.

Ahmad, K., & Wan, C. (2017). Enhanced thermoelectric performance of Bi2Te3 through uniform dispersion of single wall carbon nanotubes. *Nanotechnology*, *28*(41), 415402. https://doi.org/10.1088/1361-6528/AA810B

Ahmad, K., Wan, C., & Al-Eshaikh, M. A. (2016a). Effect of Uniform Dispersion of Single-Wall Carbon Nanotubes on the Thermoelectric Properties of BiSbTe-Based Nanocomposites. *Journal of Electronic Materials 2016 46:2*, *46*(2), 1348–1357. https://doi.org/10.1007/S11664-016-5095-Z

Ahmad, K., Wan, C., & Al-Eshaikh, M. A. (2016b). Effect of Uniform Dispersion of Single-Wall Carbon Nanotubes on the Thermoelectric Properties of BiSbTe-Based Nanocomposites. *Journal of Electronic Materials 2016 46:2*, *46*(2), 1348–1357. https://doi.org/10.1007/S11664-016-5095-Z

Ahmad, K., Wan, C., & Al-Eshaikh, M. A. (2016c). Effect of Uniform Dispersion of Single-Wall Carbon Nanotubes on the Thermoelectric Properties of BiSbTe-Based Nanocomposites. *Journal of Electronic Materials 2016 46:2*, *46*(2), 1348–1357. https://doi.org/10.1007/S11664-016-5095-Z

Akshay, V. R., Suneesh, M. V, & Vasundhara, M. (2017). Tailoring thermoelectric properties through structure and morphology in chemically synthesized n-type

bismuth telluride nanostructures. *Inorganic Chemistry*, *56*(11), 6264–6274.

Antonenko, A. O., Charnaya, E. V., Nefedov, D. Y., Podorozhkin, D. Y., Uskov, A. V., Bugaev, A. S., Lee, M. K., Chang, L. J., Naumov, S. V., Perevozchikova, Y. A., Chistyakov, V. V., Marchenkova, E. B., Weber, H. W., Huang, J. C. A., & Marchenkov, V. V. (2017). NMR studies of single crystals of the topological insulator Bi 2 Te 3 at low temperatures. *Physics of the Solid State 2017 59:5*, *59*(5), 855–859. https://doi.org/10.1134/S1063783417050031

Applications of thermoelectricity / H.J. Goldsmid. - University of Queensland. (n.d.). Retrieved October 23, 2021, from https://search.library.uq.edu.au/primo-explore/fulldisplay?vid=61UQ&docid=61UQ_ALMA2190201170003131&lang=en_US&context=L

Azhar. (2007). *Scholar (30)*. http://www.sciencedirect.com/science/article/pii/S0160738315000444

B, P., Q, H., Y, M., Y, L., A, M., B, Y., X, Y., D, W., A, M., D, V., X, C., J, L., MS, D., G, C., & Z, R. (2008). High-thermoelectric performance of nanostructured bismuth antimony telluride bulk alloys. *Science (New York, N.Y.)*, *320*(5876), 634–638. https://doi.org/10.1126/SCIENCE.1156446

Bahadar, A., & Zwawi, M. (2020). Development of SWCNTs-reinforced EPDM/SBR matrices for shock absorbing applications. *Materials Research Express*, *7*(2), 025310. https://doi.org/10.1088/2053-1591/AB71CE

Bentien, A., Johnsen, S., Madsen, G. K. H., Iversen, B. B., & Steglich, F. (2007). Colossal Seebeck coefficient in strongly correlated semiconductor FeSb2. *EPL (Europhysics Letters)*, *80*(1), 17008.

Bian, Q. (2020). Waste heat: the dominating root cause of current global warming. *Environmental Systems Research 2020 9:1*, *9*(1), 1–11.

https://doi.org/10.1186/S40068-020-00169-2

Biswas, K., He, J., Blum, I. D., Wu, C.-I., Hogan, T. P., Seidman, D. N., Dravid, V. P., & Kanatzidis, M. G. (2012). High-performance bulk thermoelectrics with all-scale hierarchical architectures. *Nature 2012 489:7416*, *489*(7416), 414–418. https://doi.org/10.1038/nature11439

Bourniquel, B., Sprauel, J. M., Feron, J., & Lebrun, J. L. (1989). Warren-Averbach Analysis of X-ray Line Profile (even truncated) Assuming a Voigt -like Profile. *International Conference on Residual Stresses*, 184–189. https://doi.org/10.1007/978-94-009-1143-7_29

Brostow, W., Datashvili, T., Lobland, H. E. H., Hilbig, T., Su, L., Vinado, C., & White, J. (2012). Bismuth telluride-based thermoelectric materials: Coatings as protection against thermal cycling effects. *Journal of Materials Research 2012 27:22*, *27*(22), 2930–2936. https://doi.org/10.1557/JMR.2012.335

Cao, Y. Q., Zhao, X. B., Zhu, T. J., Zhang, X. B., & Tu, J. P. (2008). Syntheses and thermoelectric properties of Bi2Te3⁄Sb2Te3 bulk nanocomposites with laminated nanostructure. *Applied Physics Letters*, *92*(14), 143106. https://doi.org/10.1063/1.2900960

Chang, R. P., & Rhee, S. G. (1990). (1990). *Scholar (28)*.

Chen, L. (Lidong), Liu, R., & Shi, X. (2021). *Thermoelectric materials and devices*.

Culebras, M., Igual-Muñoz, A. M., Rodríguez-Fernández, C., Gómez-Gómez, M. I., Gomez, C., & Cantarero, A. (2017). Manufacturing Te/PEDOT films for thermoelectric applications. *ACS Applied Materials & Interfaces*, *9*(24), 20826–20832.

Culebras, M., Uriol, B., Gómez, C. M., & Cantarero, A. (2015). Controlling the thermoelectric properties of polymers: application to PEDOT and polypyrrole.

Physical Chemistry Chemical Physics, *17*(23), 15140–15145. https://doi.org/10.1039/C5CP01940K

Deepa, A., Jayakrishna, K., & Rajiyalakshmi, G. (2019). Fracture surface morphologies in understanding of composite structural behavior. *Structural Health Monitoring of Biocomposites, Fibre-Reinforced Composites and Hybrid Composites*, 243–256. https://doi.org/10.1016/B978-0-08-102291-7.00012-5

Deng, Y., Zhou, X. song, Wei, G. dan, Liu, J., Nan, C. W., & Zhao, S. jing. (2002). Solvothermal preparation and characterization of nanocrystalline Bi2Te3 powder with different morphology. *Journal of Physics and Chemistry of Solids*, *63*(11), 2119–2121. https://doi.org/10.1016/S0022-3697(02)00261-5

Dimitriev, O. P., & Lashkaryov, V. (2013). Global Energy Consumption Rates: Where is the Limit? *Sustainable Energy*, *1*(1), 1–6. https://doi.org/10.12691/RSE-1-1-1

Dresselhaus, M. S., Chen, G., Tang, M. Y., Yang, R. G., Lee, H., Wang, D. Z., Ren, Z. F., Fleurial, J.-P., & Gogna, P. (2007). New Directions for Low-Dimensional Thermoelectric Materials. *Advanced Materials*, *19*(8), 1043–1053. https://doi.org/10.1002/ADMA.200600527

Du, Y., Li, J., Xu, J., & Eklund, P. (2019). Thermoelectric Properties of Reduced Graphene Oxide/Bi2Te3 Nanocomposites. *Energies 2019, Vol. 12, Page 2430*, *12*(12), 2430. https://doi.org/10.3390/EN12122430

El-Makaty, F. M., Ahmed, H. K., & Youssef, K. M. (2021). Review: The effect of different nanofiller materials on the thermoelectric behavior of bismuth telluride. *Materials & Design*, *209*, 109974. https://doi.org/10.1016/J.MATDES.2021.109974

Epp, J. (2016). X-Ray Diffraction (XRD) Techniques for Materials Characterization. *Materials Characterization Using Nondestructive Evaluation (NDE) Methods*,

81–124. https://doi.org/10.1016/B978-0-08-100040-3.00004-3

Erickson, K. J., Limmer, S. J., Yelton, W. G., Rochford, C., Siegal, M. P., & Medlin, D. L. (2017). Evolution of Microstructural Disorder in Annealed Bismuth Telluride Nanowires. *ECS Journal of Solid State Science and Technology*, *6*(3), N3117. https://doi.org/10.1149/2.0181703JSS

Fan, S., Zhao, J., Guo, J., Yan, Q., Ma, J., & Hng, H. H. (2010). p-type Bi0.4Sb1.6Te3 nanocomposites with enhanced figure of merit. *Applied Physics Letters*, *96*(18), 182104. https://doi.org/10.1063/1.3427427

Fang, H., Bahk, J.-H., Feng, T., Cheng, Z., Mohammed, A. M. S., Wang, X., Ruan, X., Shakouri, A., & Wu, Y. (2015). Thermoelectric properties of solution-synthesized n-type Bi 2 Te 3 nanocomposites modulated by Se: An experimental and theoretical study. *Nano Research 2015 9:1*, *9*(1), 117–127. https://doi.org/10.1007/S12274-015-0892-X

FJ, D. (1999). Thermoelectric cooling and power generation. *Science (New York, N.Y.)*, *285*(5428), 703–706. https://doi.org/10.1126/SCIENCE.285.5428.703

Gaikwad, M., Shevade, D., Kadam, A., & Shubham, B. (2016). Review on thermoelectric refrigeration: materials and technology. *Int J Curr Eng Technol (INPRESSCO IJCET)*, *4*(4), 67–71.

Gaul, A., Peng, Q., Singh, D. J., Ramanath, G., & Borca-Tasciuc, T. (2017). Pressure-induced insulator-to-metal transitions for enhancing thermoelectric power factor in bismuth telluride-based alloys. *Physical Chemistry Chemical Physics*, *19*(20), 12784–12793. https://doi.org/10.1039/C7CP01371J

Goldsmid, H. J. (2014). Bismuth Telluride and Its Alloys as Materials for Thermoelectric Generation. *Materials 2014, Vol. 7, Pages 2577-2592*, *7*(4), 2577–2592. https://doi.org/10.3390/MA7042577

Goldsmid, H. J. (2021). Improving the thermoelectric figure of merit. *Science and Technology of Advanced Materials*, *22*(1), 280. https://doi.org/10.1080/14686996.2021.1903816

Graupner, R. (2007). Raman spectroscopy of covalently functionalized single-wall carbon nanotubes. *Journal of Raman Spectroscopy*, *38*(6), 673–683. https://doi.org/10.1002/JRS.1694

Hines, M., Lenhardt, J., Lu, M., Jiang, L., & Xiao, Z. (2012). Cooling effect of nanoscale Bi2Te3/Sb2Te3 multilayered thermoelectric thin films. *Journal of Vacuum Science & Technology A: Vacuum, Surfaces, and Films*, *30*(4), 041509. https://doi.org/10.1116/1.4725483

Hsu, K. F. (2004). Sim Loo, Fu Guo, Wel Chen, J. Dyck, C. Uher, T. Hogan, E. Polychroniadis, M. Kanatzidis. Cubic AgPbmSbTe2+ m bulk thermoelectric materials with high figure of merit. *Science*, *203*, 818–820.

IJMS, International Journal of Mechanics Structural, Mechanics Journals, Journals Publishers, Computer Science Journals in India, Indian Journals Subscription Agency, Indian Books Distributor. (n.d.). Retrieved January 11, 2023, from https://www.ripublication.com/irph/volume/ijmsv7v1.htm

Improvement in thermoelectric properties of N-type bismuth telluride nanopowders by hydrogen reduction treatment. (n.d.). Retrieved May 17, 2022, from https://www.researchgate.net/publication/291154049_Improvement_in_thermoelectric_properties_of_N-type_bismuth_telluride_nanopowders_by_hydrogen_reduction_treatment

Ioffe, A. V, & Ioffe, A. F. (1954). Some relationships about the value of the thermal conductivity of semiconductors. *Dokl Akad Nauk SSSR*, *97*, 821.

Jian, S.-R., Le, P. H., Luo, C.-W., & Juang, J.-Y. (2017). Nanomechanical and

wettability properties of Bi2Te3 thin films: Effects of post-annealing. *Journal of Applied Physics*, *121*(17), 175302. https://doi.org/10.1063/1.4982911

Kadhim, A., Hmood, A., & Hassan, H. A. (2013). Mechanical and Electrical Properties of p-type Bi0.4Sb1.6Te3 and n-type Bi2Se0.6Te2.4 Bulk Material for Thermoelectric Applications. *Journal of Physics: Conference Series*, *431*(1), 012002. https://doi.org/10.1088/1742-6596/431/1/012002

Kaleńczuk, R., Costa, S., Borowiak-Palen, E., Kruszyńska, M., Bachmatiuk, A., & Kaleńczuk, R. J. (2008). Characterization of carbon nanotubes by Raman spectroscopy Related papers Characterization of carbon nanotubes by Raman spectroscopy. *Materials Science-Poland*, *26*(2).

Kanatzidis, M. G. (2009a). Nanostructured Thermoelectrics: The New Paradigm?†. *Chemistry of Materials*, *22*(3), 648–659. https://doi.org/10.1021/CM902195J

Kanatzidis, M. G. (2009b). Nanostructured Thermoelectrics: The New Paradigm?†. *Chemistry of Materials*, *22*(3), 648–659. https://doi.org/10.1021/CM902195J

Kanatzidis, M. G. (2010). Nanostructured thermoelectrics: The new paradigm? *Chemistry of Materials*, *22*(3), 648–659. https://doi.org/10.1021/CM902195J/ASSET/IMAGES/MEDIUM/CM-2009-02195J_0018.GIF

Keyes, R. W. (1959). High-Temperature Thermal Conductivity of Insulating Crystals: Relationship to the Melting Point. *Physical Review*, *115*(3), 564. https://doi.org/10.1103/PhysRev.115.564

Khodiri, A. A., Nawar, A. M., & Abd El-kader, K. (n.d.). Effect ofX-ray Irradiation on Structural and Optical Properties of Topological Insulator Bismuth Telluride Nano-Structure Thin Film. *IOSR Journal of Applied Physics (IOSR-JAP*, *8*, 60–68. https://doi.org/10.9790/4861-0804046068

Kim, S. Il, Lee, K. H., Mun, H. A., Kim, H. S., Hwang, S. W., Roh, J. W., Yang, D. J., Shin, W. H., Li, X. S., & Lee, Y. H. (2015). Dense dislocation arrays embedded in grain boundaries for high-performance bulk thermoelectrics. *Science*, *348*(6230), 109–114.

Kim, K. T., Choi, S. Y., Shin, E. H., Moon, K. S., Koo, H. Y., Lee, G. G., & Ha, G. H. (2013a). The influence of CNTs on the thermoelectric properties of a CNT/Bi2Te3 composite. *Carbon*, *52*, 541–549. https://doi.org/10.1016/J.CARBON.2012.10.008

Kim, K. T., Choi, S. Y., Shin, E. H., Moon, K. S., Koo, H. Y., Lee, G. G., & Ha, G. H. (2013b). The influence of CNTs on the thermoelectric properties of a CNT/Bi2Te3 composite. *Carbon*, *52*, 541–549. https://doi.org/10.1016/J.CARBON.2012.10.008

Kokalj, A. (1999). XCrySDen—a new program for displaying crystalline structures and electron densities. *Journal of Molecular Graphics and Modelling*, *17*(3–4), 176–179. https://doi.org/10.1016/S1093-3263(99)00028-5

Kumar, S., Singh, S., Dhawan, P. K., Yadav, R. R., & Khare, N. (2018). Effect of graphene nanofillers on the enhanced thermoelectric properties of Bi2Te3 nanosheets: elucidating the role of interface in de-coupling the electrical and thermal characteristics. *Nanotechnology*, *29*(13), 135703.

Lee, C. W., Kim, G. H., Choi, J. W., An, K., Kim, J., Kim, H., & Lee, Y. K. (2017). Improvement of thermoelectric properties of Bi2Te3 and Sb2Te3 films grown on graphene substrate. *Physica Status Solidi (RRL)–Rapid Research Letters*, *11*(6), 1700029.

Lemine, A. S., El-Makaty, F. M., Al-Ghanim, H. A., & Youssef, K. M. (2022). Experimental and modeling analysis of p-type Bi0.4Sb1.6Te3 and graphene

nanocomposites. *Journal of Materials Research and Technology*, *16*, 1702–1712. https://doi.org/10.1016/J.JMRT.2021.12.096

Lenz, A., Kariis, H., Pohl, A., Persson, P., & Ojamäe, L. (2011). The electronic structure and reflectivity of PEDOT:PSS from density functional theory. *Chemical Physics*, *384*(1–3), 44–51. https://doi.org/10.1016/J.CHEMPHYS.2011.05.003

Li, J., Shen, J., Ma, Z., & Wu, K. (2017). Thickness-controlled electronic structure and thermoelectric performance of ultrathin SnS2 nanosheets. *Scientific Reports 2017 7:1*, *7*(1), 1–9. https://doi.org/10.1038/s41598-017-09572-9

Liang, B., Song, Z., Wang, M., Wang, L., & Jiang, W. (2013). Fabrication and thermoelectric properties of graphene/Bi2Te 3 composite materials. *Journal of Nanomaterials*, *2013*. https://doi.org/10.1155/2013/210767

Loa, I., Bos, J.-W. G., Downie, R. A., & Syassen, K. (2016). Atomic ordering in cubic bismuth telluride alloy phases at high pressure. *Physical Review B*, *93*(22), 224109. https://doi.org/10.1103/PhysRevB.93.224109

Lognoné, Q., & Gascoin, F. (2014). Reactivity, stability and thermoelectric properties of n-Bi2Te3 doped with different copper amounts. *Journal of Alloys and Compounds*, *610*, 1–5. https://doi.org/10.1016/J.JALLCOM.2014.04.166

Lognoné, Q., & Gascoin, F. (2015). On the effect of carbon nanotubes on the thermoelectric properties of n-Bi2Te2.4Se0.6 made by mechanical alloying. *Journal of Alloys and Compounds*, *635*, 107–111. https://doi.org/10.1016/J.JALLCOM.2015.02.055

Luo, B., Deng, Y., Wang, Y., Gao, M., Zhu, W., Hashim, H. T., & García-Cañadas, J. (2016). Synergistic photovoltaic–thermoelectric effect in a nanostructured CdTe/Bi2Te3 heterojunction for hybrid energy harvesting. *RSC Advances*, *6*(115), 114046–114051. https://doi.org/10.1039/C6RA20149K

Mahmud, K. H., Yudistirani, S. A., & Ramadhan, A. I. (2017). Analysis of power characteristics of model thermoelectric generator (TEG) small modular. *International Journal of Scientific & Technology Research*, *6*(4), 161–167.

Mamur, H., Bhuiyan, M. R. A., Korkmaz, F., & Nil, M. (2018). A review on bismuth telluride (Bi2Te3) nanostructure for thermoelectric applications. *Renewable and Sustainable Energy Reviews*, *82*, 4159–4169. https://doi.org/10.1016/J.RSER.2017.10.112

Mekdad, H. N., Mahood, O. A., & Mansoor, J. M. (2020). Study of SWCNT Effect on Some Mechanical Properties of Epoxy Nanocomposites. *Diyala Journal For Pure Science*, *16*(02).

Nabi, C. K., Ahmad, K., & Al-Eshaikh, M. (n.d.). *Thermal Properties of Bismuth Antimony Telluride with Multi-Wall Carbon Nanotubes using Spark Plasma Sintering*.

Nanot, S., Thompson, N. A., Kim, J. H., Wang, X., Rice, W. D., Hároz, E. H., Ganesan, Y., Pint, C. L., & Kono, J. (2013). Single-walled carbon nanotubes. *Springer Handbook of Nanomaterials*, 105–146. https://doi.org/10.1007/978-3-642-20595-8_4

Neeli, G., Behara, D. K., & Kumar, M. K. (2016). State of the art review on thermoelectric materials. *International Journal of Science and Research*, *5*, 1833–1844.

Nozariasbmarz, A., Poudel, B., Li, W., Kang, H. B., Zhu, H., & Priya, S. (2020a). Bismuth Telluride Thermoelectrics with 8% Module Efficiency for Waste Heat Recovery Application. *IScience*, *23*(7), 101340. https://doi.org/10.1016/J.ISCI.2020.101340

Nozariasbmarz, A., Poudel, B., Li, W., Kang, H. B., Zhu, H., & Priya, S. (2020b).

Bismuth Telluride Thermoelectrics with 8% Module Efficiency for Waste Heat Recovery Application. *IScience*, *23*(7), 101340. https://doi.org/10.1016/J.ISCI.2020.101340

Oladijo, O. P., Awe, S. A., Akinlabi, E. T., Phiri, R. R., Collieus, L. L., & Phuti, R. E. (2021). High-Temperature Properties of Metal Matrix Composites. *Encyclopedia of Materials: Composites*, 360–374. https://doi.org/10.1016/B978-0-12-819724-0.00096-3

Orr, B., Akbarzadeh, A., Mochizuki, M., & Singh, R. (2016). A review of car waste heat recovery systems utilising thermoelectric generators and heat pipes. *Applied Thermal Engineering*, *101*, 490–495. https://doi.org/10.1016/J.APPLTHERMALENG.2015.10.081

Ouyang, Y., Cong, L. M., Chen, L., Liu, Q. X., & Fang, Y. (2008). Raman study on single-walled carbon nanotubes and multi-walled carbon nanotubes with different laser excitation energies. *Physica E: Low-Dimensional Systems and Nanostructures*, *40*(7), 2386–2389. https://doi.org/10.1016/J.PHYSE.2007.11.008

Park, J. G., & Lee, Y. H. (2016). High thermoelectric performance of Bi-Te alloy: Defect engineering strategy. *Current Applied Physics*, *9*(16), 1202–1215. https://doi.org/10.1016/J.CAP.2016.03.028

Peng, Y. Y., Dussan, D. D., & Narain, R. (2020). Thermal, mechanical, and electrical properties. *Polymer Science and Nanotechnology: Fundamentals and Applications*, 179–201. https://doi.org/10.1016/B978-0-12-816806-6.00009-1

Pezzoli, F., Deneke, C., & Schmidt, O. G. (2011). Strain engineering of silicon–germanium (SiGe) micro- and nanostructures. *Silicon-Germanium (SiGe) Nanostructures*, 247–295. https://doi.org/10.1533/9780857091420.2.247

Pinto, A. M. F. R., Oliveira, V. B., & Falcão, D. S. (2018). Experimental methods of characterization. *Direct Alcohol Fuel Cells for Portable Applications*, 113–155. https://doi.org/10.1016/B978-0-12-811849-8.00004-8

Poudel, B., Hao, Q., Ma, Y., Lan, Y., Minnich, A., Yu, B., Yan, X., Wang, D., Muto, A., Vashaee, D., Chen, X., Liu, J., Dresselhaus, M. S., Chen, G., & Ren, Z. (2008). High-Thermoelectric Performance of Nanostructured Bismuth Antimony Telluride Bulk Alloys. *Science*, *320*(5876), 634–638. https://doi.org/10.1126/SCIENCE.1156446

Rakhi, R. B. (2019). Preparation and properties of manipulated carbon nanotube composites and applications. *Nanocarbon and Its Composites: Preparation, Properties and Applications*, 489–520. https://doi.org/10.1016/B978-0-08-102509-3.00016-X

Raman, C. V., & Krishnan, K. S. (1928). A New Type of Secondary Radiation. *Nature 1928 121:3048*, *121*(3048), 501–502. https://doi.org/10.1038/121501c0

Rodríguez-Fernández, C., Manzano, C. V, Romero, A. H., Martín, J., Martín-González, M., Jr, M. M. de L., & Cantarero, A. (2016). The fingerprint of Te-rich and stoichiometric Bi2Te3 nanowires by Raman spectroscopy. *Nanotechnology*, *27*(7), 075706. https://doi.org/10.1088/0957-4484/27/7/075706

Saifuddin, N., Raziah, A. Z., & Junizah, A. R. (2013). Carbon nanotubes: A review on structure and their interaction with proteins. *Journal of Chemistry*. https://doi.org/10.1155/2013/676815

Saleemi, M., Toprak, M. S., Li, S., Johnsson, M., & Muhammed, M. (2011). Synthesis, processing, and thermoelectric properties of bulk nanostructured bismuth telluride (Bi2Te3). *Journal of Materials Chemistry*, *22*(2), 725–730. https://doi.org/10.1039/C1JM13880D

Satterthwaite, C. B., & R. W. Ure, J. (1957). Electrical and Thermal Properties of <span class. *Physical Review*, *108*(5), 1164. https://doi.org/10.1103/PhysRev.108.1164

Scheele, M., Oeschler, N., Meier, K., Kornowski, A., Klinke, C., & Weller, H. (2009). Synthesis and Thermoelectric Characterization of Bi2Te3 Nanoparticles. *Advanced Functional Materials*, *19*(21), 3476–3483. https://doi.org/10.1002/ADFM.200901261

scholar (29). (n.d.).

Sharma, S., Stello, D., & Bland-Hawthorn, J. (2016). Modelling the Milky Way with Galaxia and making use of asteroseismology. *Astronomische Nachrichten*, *337*(8–9), 875–879. https://doi.org/10.1002/ASNA.201612389

Singh, D. J., & Terasaki, I. (2008). Nanostructuring and more. *Nature Materials 2008 7:8*, *7*(8), 616–617. https://doi.org/10.1038/nmat2243

Singh, S., Kumar, A., & Singh, D. (2020). Enhanced Microwave Absorption Performance of SWCNT/SiC Composites. *Journal of Electronic Materials 2020 49:12*, *49*(12), 7279–7291. https://doi.org/10.1007/S11664-020-08460-9

Smekal, A. (1923). Zur quantentheorie der dispersion. *Naturwissenschaften*, *11*(43), 873–875.

Smith, E., & Dent, G. (n.d.). *Modern Raman spectroscopy : a practical approach*. Retrieved January 26, 2022, from https://www.wiley.com/en-us/Modern+Raman+Spectroscopy%3A+A+Practical+Approach%2C+2nd+Edition-p-9781119440550

Smith, R. L., & Sandland, G. E. (1922). An accurate method of determining the hardness of metals, with particular reference to those of a high degree of hardness.** a prize of £20 was awarded to each author by the Sir Robert Hadfield prize committee. *Proceedings of the Institution of Mechanical Engineers*, *102*(1),

623–641. https://doi.org/10.1243/PIME_PROC_1922_102_033_02

Snyder, G. J., & Toberer, E. S. (2008). Complex thermoelectric materials. *Nature Materials 2008 7:2*, *7*(2), 105–114. https://doi.org/10.1038/nmat2090

Sootsman, J. R., Chung, D. Y., & Kanatzidis, M. G. (2009). New and Old Concepts in Thermoelectric Materials. *Angewandte Chemie International Edition*, *48*(46), 8616–8639. https://doi.org/10.1002/ANIE.200900598

Suryanarayana, C. (2004). *Mechanical alloying and milling*. 466.

Suzuki, S., & Hibino, H. (2011). Characterization of doped single-wall carbon nanotubes by Raman spectroscopy. *Carbon*, *49*(7), 2264–2272. https://doi.org/10.1016/J.CARBON.2011.01.059

Takashiri, M., Takiishi, M., Tanaka, S., Miyazaki, K., & Tsukamoto, H. (2007). Thermoelectric properties of n-type nanocrystalline bismuth-telluride-based thin films deposited by flash evaporation. *Journal of Applied Physics*, *101*(7), 074301. https://doi.org/10.1063/1.2717867

Talebi, T., Ghomashchi, R., Talemi, P., & Aminorroaya Yamini, S. (2017). Preparation of n-type Bi2Te3 films by electrophoretic deposition. *International Journal of Chemical, Molecular, Nuclear, Materials and Metallurgical Engineering*, *11*(4).

Tan, G., Ohta, M., & Kanatzidis, M. G. (2019a). Thermoelectric power generation: from new materials to devices. *Philosophical Transactions of the Royal Society A*, *377*(2152). https://doi.org/10.1098/RSTA.2018.0450

Tan, G., Ohta, M., & Kanatzidis, M. G. (2019b). Thermoelectric power generation: From new materials to devices. *Philosophical Transactions of the Royal Society A: Mathematical, Physical and Engineering Sciences*, *377*(2152), 20180450. https://doi.org/10.1098/RSTA.2018.0450

Tanaka, S., Takiishi, M., Miyazaki, K., & Tsukamoto, H. (2009). Measurements of

Thermal Conductivity of Thin Films by 3-Omega Method. *2008 Proceedings of the ASME Micro/Nanoscale Heat Transfer International Conference, MNHT 2008, PART A*, 477–483. https://doi.org/10.1115/MNHT2008-52260

Tang, X., Xie, W., Li, H., Zhao, W., Zhang, Q., Niino, M., Tang, X., Xie, W., Li, H., Zhao, W., Zhang, Q., & Niino, M. (2007). Preparation and thermoelectric transport properties of high-performance p-type Bi₂Te₃ with layered nanostructure. *ApPhL*, *90*(1), 012102. https://doi.org/10.1063/1.2425007

Technology, I.-I. J. for I. R. in S. and. (n.d.). *A Review on Thermoelectric Cooler*. Retrieved July 21, 2021, from https://www.academia.edu/25849293/A_Review_on_Thermoelectric_Cooler

TEM: Bright field versus dark field - Chemistry LibreTexts. (n.d.). Retrieved January 26, 2022, from https://chem.libretexts.org/Courses/Franklin_and_Marshall_College/Introduction_to_Materials_Characterization__CHM_412_Collaborative_Text/Electron_and_Probe_Microscopy/TEM%3A_Bright_field_versus_dark_field

Thermal Conductivity | Open Science Wiki | Fandom. (n.d.). Retrieved April 9, 2022, from https://science.fandom.com/wiki/Thermal_Conductivity

Thermoelectric Materials and Devices - 1st Edition. (n.d.). Retrieved October 22, 2022, from https://www.elsevier.com/books/thermoelectric-materials-and-devices/chen/978-0-12-818413-4

Thermoelectric Materials and Devices - Lidong Chen, Ruiheng Liu, Xui Shi - Google Books. (n.d.). Retrieved October 20, 2021, from https://books.google.com.qa/books?id=p5vgDwAAQBAJ&pg=PA224&lpg=PA224&dq=This+Y-

shaped+structure+can+more+readily+accommodate+TE+elements+with+different+thickness,+cross-sectional+area,+and+CTE.+The+p-+and+n+type+THE+elements+are+arranged+alternately+with+inserting+an+electrode+between+the+neighboring+elements.+The+electrodes+also+facilitate+the+thermal+transport+from+the+heat+source+to+the+side+TE+elements+in+a+cornering+transfer+trajectory.+This+Y-shaped+structure+allows+integration+of+TE+elements+with+unconstrained+geometries,+that+is,+the+p-+and+n-type+elements+can+be+designed+in+different+shapes+and+sizes.+Furthermore,+the+TE+materials+are+stress-free,+because+TE+elements+remain+relatively+independent+and+the+stresses+are+applied+on+the+electrodes+and+insulation+components.+Each+TE+element+can+be+optimized+independently+or+partially+independently,+which+is+particularly+favorable+for+the+segmented+module.+Specifically,+each+p-+and+n-type+leg+can+have+a+different+cross-sectional+area+and/or+thickness+with+each+layer+optimized+to+reach+the+highest+ZT+in+their+particular+temperature+range.&source=bl&ots=9hMRgVg5RW&sig=ACfU3U254eYVpk5S6Cxl27tgLQXadDR5qw&hl=en&sa=X&ved=2ahUKEwj96sXD6dnzAhUPyYUKHTLQCEMQ6AF6BAgCEAM#v=onepage&q=This Y-shaped structure can more readily accommodate TE elements with different thickness%2C cross-sectional area%2C and CTE. The p- and n type THE elements are arranged alternately with inserting an electrode between the neighboring elements. The electrodes also facilitate the thermal transport from the heat source to the side TE elements in a cornering transfer trajectory. This Y-shaped structure allows integration of TE elements with unconstrained

geometries%2C that is%2C the p- and n-type elements can be designed in different shapes and sizes. Furthermore%2C the TE materials are stress-free%2C because TE elements remain relatively independent and the stresses are applied on the electrodes and insulation components. Each TE element can be optimized independently or partially independently%2C which is particularly favorable for the segmented module. Specifically%2C each p- and n-type leg can have a different cross-sectional area and%2For thickness with each layer optimized to reach the highest ZT in their particular temperature range.&f=false

transmission electron microscope | instrument | Britannica. (n.d.). Retrieved January 26, 2022, from https://www.britannica.com/technology/transmission-electron-microscope

Venkatasubramanian, R., Siivola, E., Colpitts, T., & O'quinn, B. (2001). Thin-film thermoelectric devices with high room-temperature figures of merit. *Nature*, *413*(6856), 597–602.

Wang, S. Q., Ma, P. C., Kim, J. K., & Tang, B. Z. (2009). In-situ amino functionalization of carbon nanotubes using ball milling. *Journal of Nanoscience and Nanotechnology*, *9*(2), 749–753. https://doi.org/10.1166/JNN.2009.C017

What are Composites? - Romeo RIM. (n.d.). Retrieved January 11, 2023, from https://romeorim.com/what-are-composites/

Wu, K., Yan, Y., Zhang, J., Mao, Y., Xie, H., Yang, J., Zhang, Q., Uher, C., & Tang, X. (2017). Preparation of n-type Bi2Te3 thermoelectric materials by non-contact dispenser printing combined with selective laser melting. *Physica Status Solidi (RRL)–Rapid Research Letters*, *11*(6), 1700067.

Xie, W., Tang, X., Yan, Y., Zhang, Q., & Tritt, T. M. (2009a). Unique nanostructures and enhanced thermoelectric performance of melt-spun BiSbTe alloys. *Applied*

Physics Letters, *94*(10), 102111. https://doi.org/10.1063/1.3097026

Xie, W., Tang, X., Yan, Y., Zhang, Q., & Tritt, T. M. (2009b). Unique nanostructures and enhanced thermoelectric performance of melt-spun BiSbTe alloys. *Applied Physics Letters*, *94*(10), 102111. https://doi.org/10.1063/1.3097026

Xie, W., Tang, X., Yan, Y., Zhang, Q., & Tritt, T. M. (2009c). High thermoelectric performance BiSbTe alloy with unique low-dimensional structure. *Journal of Applied Physics*, *105*(11), 113713. https://doi.org/10.1063/1.3143104

Yu, M. F., Files, B. S., Arepalli, S., & Ruoff, R. S. (2000). Tensile Loading of Ropes of Single Wall Carbon Nanotubes and their Mechanical Properties. *Physical Review Letters*, *84*(24), 5552. https://doi.org/10.1103/PhysRevLett.84.5552

Zhang, C., Fan, X. A., Hu, J., Jiang, C., Xiang, Q., Li, G., Li, Y., & He, Z. (2017). Changing the Band Gaps by Controlling the Distribution of Initial Particle Size to Improve the Power Factor of N-Type Bi2Te3 Based Polycrystalline Bulks. *Advanced Engineering Materials*, *19*(8), 1600696.

Zhang, Y., Wang, X. L., Yeoh, W. K., Zeng, R. K., & Zhang, C. (2012). Electrical and thermoelectric properties of single-wall carbon nanotube doped Bi2Te3. *Applied Physics Letters*, *101*(3), 031909. https://doi.org/10.1063/1.4737898

Zhao, X. B., Ji, X. H., Zhang, Y. H., Zhu, T. J., Tu, J. P., & Zhang, X. B. (2005a). Bismuth telluride nanotubes and the effects on the thermoelectric properties of nanotube-containing nanocomposites. *Applied Physics Letters*, *86*(6), 062111. https://doi.org/10.1063/1.1863440

Zhao, X. B., Ji, X. H., Zhang, Y. H., Zhu, T. J., Tu, J. P., & Zhang, X. B. (2005b). Bismuth telluride nanotubes and the effects on the thermoelectric properties of nanotube-containing nanocomposites. *Applied Physics Letters*, *86*(6), 062111. https://doi.org/10.1063/1.1863440

Zheng, Y., Tan, X. Y., Wan, X., Cheng, X., Liu, Z., & Yan, Q. (2020). Thermal Stability and Mechanical Response of Bi2Te3-Based Materials for Thermoelectric Applications. *ACS Applied Energy Materials*, *3*(3), 2078–2089. https://doi.org/10.1021/ACSAEM.9B02093/ASSET/IMAGES/MEDIUM/AE9B02093_0011.GIF

Zuo, G., Abdalla, H., & Kemerink, M. (2016). Impact of doping on the density of states and the mobility in organic semiconductors. *Physical Review B*, *93*(23), 235203. https://doi.org/10.1103/PhysRevB.93.235203